

A human brain map of mitochondrial respiratory capacity and diversity

<https://doi.org/10.1038/s41586-025-08740-6>

Received: 8 March 2024

Accepted: 4 February 2025

Published online: 26 March 2025

 Check for updates

Eugene V. Mosharov^{1,2}, Ayelet M. Rosenberg^{1,12}, Anna S. Monzel^{1,12}, Corey A. Osto³, Linsey Stiles³, Gorazd B. Rosoklija^{2,4}, Andrew J. Dwork^{2,4,5}, Snehal Bindra¹, Alex Junker¹, Ya Zhang⁶, Masashi Fujita⁶, Madeline B. Mariani^{2,4}, Mihran Bakalian^{2,4}, David Sulzer^{1,2,7}, Philip L. De Jager⁶, Vilas Menon⁶, Orian S. Shirihi³, J. John Mann^{2,4}, Mark D. Underwood^{2,4}, Maura Boldrini^{2,4}, Michel Thiebaut de Schotten^{8,9} & Martin Picard^{1,2,10,11}

Mitochondrial oxidative phosphorylation (OXPHOS) powers brain activity^{1,2}, and mitochondrial defects are linked to neurodegenerative and neuropsychiatric disorders^{3,4}. To understand the basis of brain activity and behaviour, there is a need to define the molecular energetic landscape of the brain^{5–10}. Here, to bridge the scale gap between cognitive neuroscience and cell biology, we developed a physical voxelization approach to partition a frozen human coronal hemisphere section into 703 voxels comparable to neuroimaging resolution (3 × 3 × 3 mm). In each cortical and subcortical brain voxel, we profiled mitochondrial phenotypes, including OXPHOS enzyme activities, mitochondrial DNA and volume density, and mitochondria-specific respiratory capacity. We show that the human brain contains diverse mitochondrial phenotypes driven by both topology and cell types. Compared with white matter, grey matter contains >50% more mitochondria. Moreover, the mitochondria in grey matter are biochemically optimized for energy transformation, particularly among recently evolved cortical brain regions. Scaling these data to the whole brain, we created a backwards linear regression model that integrates several neuroimaging modalities¹¹ to generate a brain-wide map of mitochondrial distribution and specialization. This model predicted mitochondrial characteristics in an independent brain region of the same donor brain. This approach and the resulting MitoBrainMap of mitochondrial phenotypes provide a foundation for exploring the molecular energetic landscape that enables normal brain function. This resource also relates to neuroimaging data and defines the subcellular basis for regionalized brain processes relevant to neuropsychiatric and neurodegenerative disorders. All data are available at <http://humanmitobrainmap.bcblab.com>.

Functional neuroimaging techniques capture dynamic electrical, metabolic and haemodynamic brain energy states^{12–15} but provide only indirect measures of the underlying subcellular bioenergetic processes. All basal and activity-dependent brain processes depend on cellular energy transformation, or bioenergetics, involving ATP synthesis by oxidative phosphorylation (OXPHOS) in trillions of respiring mitochondria¹⁶. There are hundreds to thousands of these organelles per neuron and glial cell¹⁷. Mitochondria are molecularly specialized to meet specific cellular demands, direct subcellular activities^{5,6,17–19} and provide the necessary energy to support brain activity.

Beyond energetics, mitochondria participate in other crucial functions, including cell–cell signalling²⁰ and regulation of neuronal excitability²¹, neurotransmitter release²² and modulation of inflammatory processes^{23,24}. Consequently, mitochondria also have a vital role in numerous supporting functions distributed across the large-scale networks of the brain. Recent mechanistic studies have highlighted the influence of mitochondria on cognition^{25,26} and behaviour^{27,28}. However, mitochondria are typically examined at the submicron scale in cell biology, which represents a major methodological and conceptual scale gap with cognitive and systems neuroscience. This field operates at

¹Department of Psychiatry, Divisions of Molecular Therapeutics and Behavioral Medicine, Columbia University Irving Medical Center, New York, NY, USA. ²New York State Psychiatric Institute, New York, NY, USA. ³Department of Medicine, Endocrinology, and Department of Molecular and Medical Pharmacology, David Geffen School of Medicine, University of California Los Angeles, Los Angeles, CA, USA. ⁴Department of Psychiatry, Division of Molecular Imaging and Neuropathology, Columbia University Irving Medical Center, New York, NY, USA. ⁵Department of Pathology and Cell Biology, Columbia University, New York, NY, USA. ⁶Center for Translational and Computational Neuroimmunology, Neuroimmunology Division, Department of Neurology and the Taub Institute for Research on Alzheimer's Disease and the Aging Brain, Columbia University Irving Medical Center, New York, NY, USA. ⁷Departments of Neurology and Pharmacology, Columbia University Irving Medical Center, New York, NY, USA. ⁸Brain Connectivity and Behaviour Laboratory, Paris, France. ⁹Groupe d'Imagerie Neurofonctionnelle, Institut des Maladies Neurodégénératives-UMR 5293, CNRS, CEA University of Bordeaux, Bordeaux, France. ¹⁰Department of Neurology, H. Houston Merritt Center, Columbia Translational Neuroscience Initiative, Columbia University Irving Medical Center, New York, NY, USA. ¹¹Robert N. Butler Columbia Aging Center, Columbia University Mailman School of Public Health, New York, NY, USA. ¹²These authors contributed equally: Ayelet M. Rosenberg, Anna S. Monzel. [✉]e-mail: michel.thiebaut@gmail.com; martin.picard@columbia.edu

Article

the scale of millimetres when the whole brain is imaged by magnetic resonance imaging (MRI) at conventional field strength. Therefore, a major obstacle keeping us from resolving the energetic forces that power and direct complex human brain dynamics is the spatial distribution of energy-transforming mitochondria across brain structures.

Neuroimaging techniques are invaluable for mapping brain metabolism on a large scale. Positron emission tomography (PET) provides quantitative measurements of metabolic processes, including glucose metabolism using [¹⁸F]-FDG, but requires invasive radioactive tracers and has limited spatial resolution²⁹. Blood oxygen level dependent (BOLD) functional MRI (fMRI) captures variations in haemoglobin oxygenation at millimetre and second resolution, but it only indirectly reflects the mixed contribution of metabolic (aerobic and anaerobic) responses to brain tissue activity³⁰. Chemical exchange saturation transfer (CEST) MRI maps metabolites by detecting exchangeable biomolecule protons at a relatively high spatial resolution, but faces limits to quantify absolute metabolite concentrations³¹. Functional magnetic resonance spectroscopy (fMRS) quantifies neurotransmitter and metabolite concentrations such as glutamate and lactate to provide insights into *in vivo* brain metabolism. However, low signal-to-noise ratio limits its temporal and spatial resolution, which requires large voxel sizes during acquisition³². These and the integration of other techniques (for example, those that measure the cerebral metabolic rate of oxygen or the cerebral blood volume^{9,33,34}) provide a broad view of brain metabolism in relation to function. However, their interpretation requires the development of high-resolution, brain-wide map of the molecular energetic landscape, which is crucial for understanding regional metabolic properties and energy-transformation capacity. Such a map would enable the integration of mitochondrial bioenergetics with macroscopic neuroimaging data, thereby potentially enhancing the specificity of metabolic assessments from PET, BOLD fMRI, CEST MRI and fMRS by linking them to mitochondrial biology.

Preliminary work has begun to bridge mesoscale neuroimaging with microscopic anatomy, which has provided breakthroughs for cellular imaging interpretation of human neuroimaging findings^{35–37}. Such advancements aspire to inform our understanding of brain development, cognition, mood and the mechanisms that underlie various neuropathologies. To connect cognitive neuroscience and cell biology, here we develop a method to physically voxelize frozen human brain tissue to systematically profile mitochondrial molecular and biochemical diversity across a coronal brain section. We also provide an algorithm for predicting mitochondrial distribution, density and OXPHOS capacity based on common MRI data.

Brain voxelization

To systematically map mitochondrial distribution, diversity and molecular specialization across the human brain, the first challenge was to physically partition frozen brain tissue at a spatial resolution comparable to MRI. This would enable the mapping of molecular and biochemical profiles to standard neuroimaging stereotaxic space (Fig. 1a).

To address this challenge, we selected a neurotypical brain obtained within a short post-mortem interval (PMI = 8 h, storage at -80°C for 10 years). The donor was a 54-year-old man with a negative toxicology screen for psychoactive medication, drugs and alcohol, negative neuropathology and negative history of a neuropsychiatric disorder (Methods). A coronal slab of the entire right hemisphere, including cortical and subcortical anatomical structures, was voxelized while maintained frozen at -25°C to preserve enzyme activities and molecular integrity during processing. To physically partition the frozen brain slab at 3 mm isotropic resolution, comparable to MRI, we programmed a computer numerical control (CNC) cutter to engrave a $3 \times 3 \text{ mm}$ square grid at 3 mm depth, followed by manual collection and indexing of a total of 703 samples (Extended Data Figs. 1 and 2 and Supplementary Video 1).

Phenotyping of brain mitochondria

To perform mitochondrial phenotyping at a scale of hundreds of physical human brain voxels, each sample was first randomly assigned to a well across 96-well plates (later deconvolved using a custom algorithm; Extended Data Fig. 2 and Methods), weighed, homogenized and subjected to quality control and basic characterization of total protein concentration and nuclear DNA content. These parameters demonstrated relatively uniform quality across the brain section (Fig. 1b–d). The average voxel weight was $26.2 \pm 4.5 \text{ mg}$ (mean \pm s.d.; predicted weight = 27 mg from $3 \times 3 \times 3 \text{ mm}$ voxel dimensions at aqueous volumetric density). Such small tissue samples require high-sensitivity assays for both mitochondrial density and enzymatic activities of the respiratory chain (also known as the electron transport chain (ETC))⁵. Mitochondrial density was assessed using a combination of two mitochondrial markers: citrate synthase (CS) activity and mitochondrial DNA (mtDNA) density. OXPHOS enzymes that reflect energy-transformation capacity were indexed using three markers: complex I (CI; also known as NADH–ubiquinone oxidoreductase); complex II (CII; also known as succinate dehydrogenase (SDH)); and complex IV (CIV; also known as cytochrome c oxidase (COX)). These enzymes transport electrons and generate the life-giving transmembrane potential that ultimately powers ATP synthesis by the OXPHOS system²⁰.

To ensure the robustness of the data, OXPHOS enzymatic activities were quantified using two independent assays in different laboratories: a miniaturized colourimetric assay optimized for brain tissue⁵ and frozen-tissue respirometry^{38,39} (Extended Data Fig. 2). To increase technical accuracy across the dataset, standard reference samples from the occipital lobe of the same brain (grey matter (GM), white matter (WM) and voxels of mixed GM and WM composition) that spanned the spectrum of possible activities were assayed in duplicate in each batch (eight 96-well assay plates) and used to correct for potential batch effects. This process resulted in a uniform MRI-resolution dataset of mitochondrial activity profiles across the entire coronal section of the human brain (Extended Data Fig. 3a–f). We excluded voxels with either too little tissue (samples located at the edges of the brain section) or enzymatic activities below the detection limit (mainly from the WM), which led to around 10% of the voxels missing at least one measure. All mitochondrial features (CI, CII, CIV, CS and mtDNA) were determined in 633 voxels, which required 27,820 individual samples analysed by colourimetric, respirometry, biochemical and quantitative PCR (qPCR) assays, including replicates, controls and standards (Methods).

Mitochondria density and OXPHOS capacity

Mitochondria have molecular and functional specialties and exhibit a wide range of energy-transformation capacities¹⁸. To assess mitochondrial ‘quality’ and functional specialization, we previously developed a simple linear formula in which OXPHOS activities are divided by mitochondrial mass to produce an index of OXPHOS capacity on a per mitochondrion basis, which we called the mitochondrial health index (MHI)⁴⁰. Here with a substantially larger brain mitochondrial biochemistry dataset at hand, we discovered that the distributions of individual mitochondrial metrics were left-skewed (Extended Data Fig. 4a).

When spheroid organelles have normally distributed radii, metrics related to the surface area of the spheroid follow a square-root normal distribution, whereas those related to the volume of the spheroid are cube-root normalized. A well-established example of such dependence is observed with dense core secretory vesicles in which a similarly left-skewed distribution of neurotransmitter content is normalized by a cube-root transformation⁴¹. Although the morphology of mitochondria is more complex than a sphere, volumetric transformation of mitochondrial content ($\text{CS}^{1/3}$ and $\text{mtDNA}^{1/3}$) and OXPHOS capacity ($\text{CI}^{1/2}$,

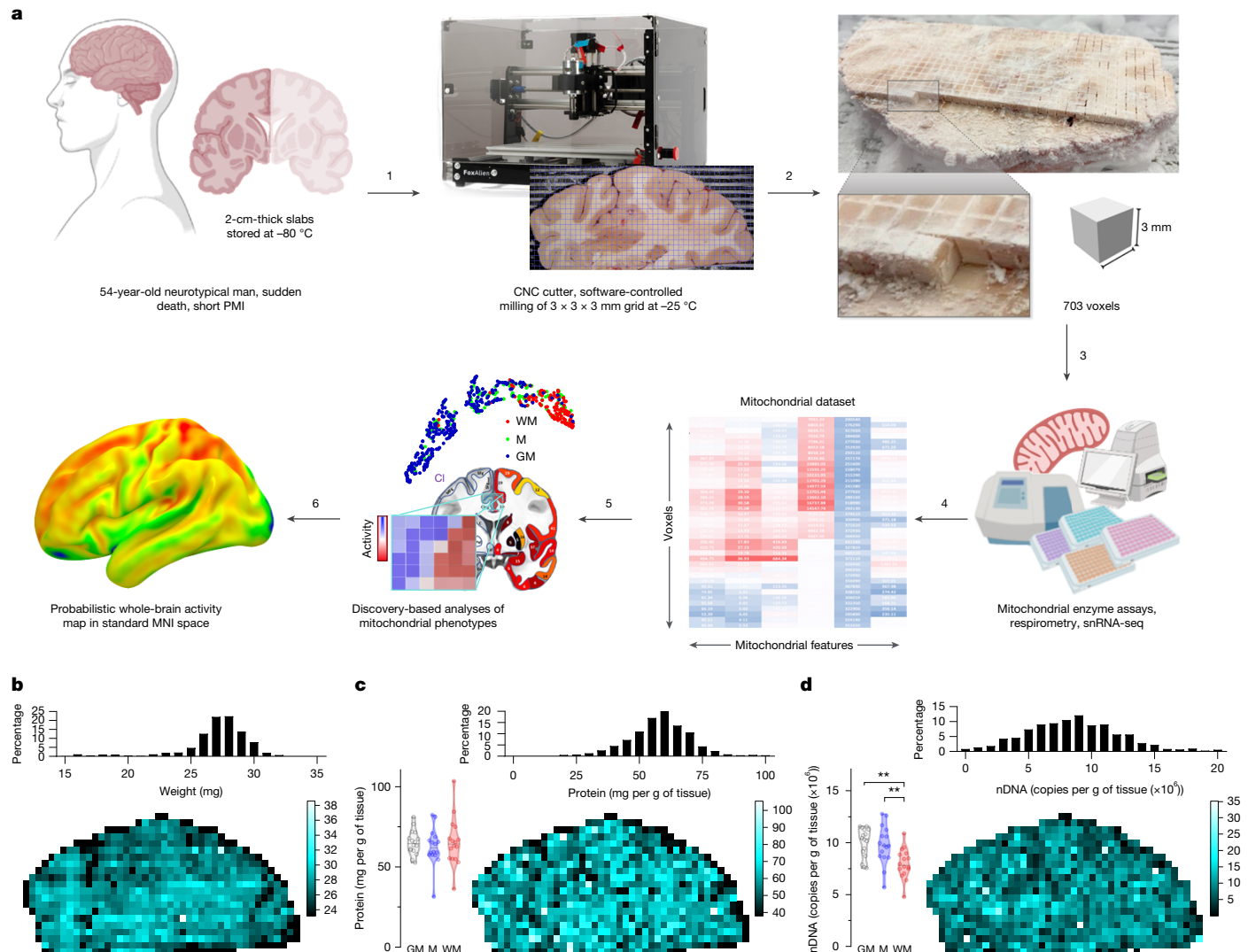


Fig. 1 | Human brain voxelization and mapping. **a**, Post-mortem brain tissue was sectioned into around 2-cm-thick coronal slabs, flash-frozen in the refrigerant R-134a and stored at -80 °C for 10 years (Methods). A slab located at stereotactic MNI coordinates 15.51 mm posterior to the centre of the anterior commissure⁶¹ was mounted on a CNC cutter operated in a -25 °C freezer room (step 1). The top surface was cleaned and levelled, and a 3 × 3 mm grid was milled with a 0.4 mm drill bit to the depth of 3 mm (step 2). Brain voxels were manually collected, the surface cleaned once more, and several 50 nm cryosections were collected for histological evaluation. Each of the >700 samples was weighed, homogenized and ran through an array of biochemical tests to generate matrices of mitochondrial features linked to voxel coordinates on the brain slice (step 3). Each voxel was characterized on the basis of relative activities and abundance of mitochondrial complexes (step 4). Dimensionality reduction and clustering analyses were performed to identify different mtotypes (step 5). Maps of mitochondrial features were registered onto a standard MNI space and

regression analyses were performed to relate these maps to the average MRI readouts for the same brain regions. Finally, MRI data were used to predict mitochondrial features and to extend mitochondrial maps to the whole brain (step 6). Created in BioRender. Mosharov, E. (2025) <https://BioRender.com/z524941>. **b–d**, Basic properties of collected voxels, including their weight (**b**), protein content (**c**) and nuclear DNA (nDNA) content (**d**). Histograms of each parameter values are shown on top and mapping of values on the brain slice at the bottom. Bar graphs on the left of the brain slice show repeated measurements of the corresponding values in control GM, WM and mixed (M) GM and WM matter samples from the occipital lobe of the same brain that were used as normalization controls in the assay plates (Extended Data Fig. 2d). Note that the colour bars in each panel use the same label as the x-axis label of their corresponding histogram. ** $P < 0.01$ by one-way analysis of variance (ANOVA) with Tukey's post hoc test.

$\text{CII}^{1/2}$ and $\text{CIV}^{1/2}$) parameters adequately normalized the mitochondrial features (that is, decreased coefficients of variation, skewness and Kolmogorov–Smirnov distance). This transformation also enabled us to deconvolve the normal distributions of mitochondrial features for both GM and WM voxels to produce a final parametric dataset of individual mitochondrial features (Extended Data Fig. 4b–d).

As expected, the transformed mitochondrial content markers were strongly correlated (Pearson's $r^2 = 0.46$, $P < 0.0001$; Extended Data Fig. 5a), which provided a basis for the integration of $\text{CS}^{1/3}$ and mtDNA $^{1/3}$ as MitoD, which represents the mitochondria tissue density for each brain voxel (Fig. 2a,c). The mtDNA copy number (mtDNAcn),

which reflects the number of mtDNA genomes per cell nucleus, is also presented (Extended Data Fig. 3h) but is influenced by cellularity; therefore, comparisons between brain regions cannot be straightforward⁶. Activities of OXPHOS enzymes measured by colourimetric and respirometry assays were also highly correlated (Extended Data Fig. 5b–d), and these were subsequently averaged to integrate them as a robust measure of tissue respiratory capacity (TRC; Fig. 2a,b). The TRC represents the direct quantification of mitochondrial OXPHOS capacity per mg of brain tissue.

Reference GM voxels exhibited significantly higher values for all mitochondrial metrics than reference WM voxels, with intermediate values

Article

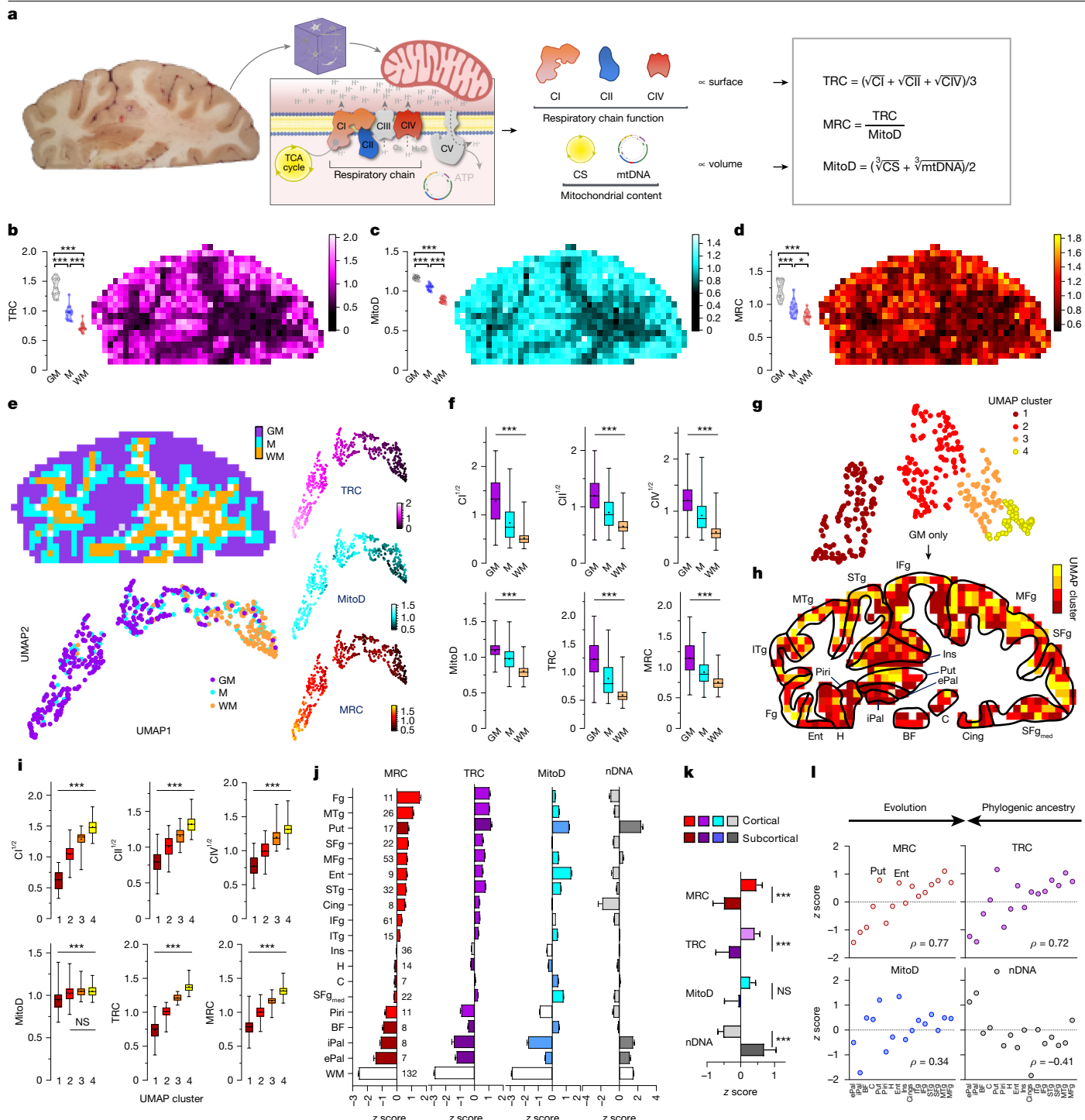


Fig. 2 | Mitochondrial density and activity of respiratory complexes.

a, Overview of enzyme activity assays. Left, brain slab before voxelization and schematic of the inner mitochondria membrane with respiratory chain complexes. Middle, relationships between organelle geometry, activities of respiratory complexes and CS and mtDNA density. Right, formulae for TRC, MRC and MitoD. Created in BioRender. Mosharov, E. (2025) <https://BioRender.com/z524941>. **b-d**, Maps of TRC (**b**; derived from Extended Data Fig. 3i,j), MitoD (**c**; average of two panels in Extended Data Fig. 3g) and MRC (**d**). Bar graphs on the left side of each panel show distributions of repeated measures of control GM, WM and mixed GM and WM samples on different assay plates. **e**, On the basis of MNI space location, 633 voxels with all 6 mitochondrial features were divided into GM ($n = 325$), WM ($n = 132$) and mixed ($n = 176$) GM and WM clusters. UMAP plots show the correlation between clusters and the physical location of each voxel (left) or z-score values of the TRC, the MitoD and the MRC

in each voxel (right). Colour bars in **b-e** show z scores of the values displayed in each panel. **f**, Bars and whiskers plots of mitochondrial features in GM, WW and mixed GM and WM voxels. **g**, UMAP plot and clusters of mitochondrial features of GM voxels. **h**, Mapping of UMAP clusters to specific brain areas (see Methods for abbreviations). **i**, Mitochondrial features in GM clusters from **g**. For MitoD, only cluster 1 is different from other clusters. **j**, Mitochondrial features in groups of voxels (group sizes are shown next to the bars) mapped to specific brain areas. Subcortical areas are in darker shades. **k**, Mitochondrial features in cortical and subcortical areas. **l**, Comparison between measured values and known phylogenetic organization of brain regions derived from comparative anatomy studies (Methods). p is Spearman's rho. * $P < 0.05$ and *** $P < 0.001$ by ANOVA with Tukey's post hoc test (**f,i**) or t-test (**k**). NS, not significant. Bar and whisker plots show 25th to 75th percentile (box), minimal and maximal values (whiskers), the median (horizontal line inside the bar) and the mean (+).

in voxels of mixed GM and WM composition (Fig. 2b,c and Extended Data Fig. 3, bar graphs on the left of each panel). This result is in agreement with previous neuroimaging-based estimates of brain energy metabolism^{5–10}. The data distributions for reference GM and WM voxels did not overlap, which highlighted their divergence. As a result, the signal-to-noise ratio to detect differences between GM and WM areas was high, as reflected by the large effect sizes for all mitochondrial metrics (Hedges' $g = 3.5\text{--}10.7$ for GM versus WM). Compared to the protein and cellularity measures that were homogenously distributed across the section (Fig. 1b–d), the maps of mitochondrial features (Fig. 2b,c and Extended Data Fig. 3g–j) showed clear heterogeneity that overlapped with brain anatomy (Fig. 2a).

To create a volumetric analogue of the MHI that reflects tissue-specific specialization of mitochondria for OXPHOS and energy transformation, we computed an additional metric that we labelled the mitochondrial respiratory capacity (MRC) by expressing the TRC relative to the MitoD (MRC = TRC/MitoD) for each voxel (Fig. 2a). If each mitochondrion across the brain section had the same OXPHOS energy-transformation capacity, then the MRC should have similar values in all brain areas. Conversely, a difference in the MRC would indicate the presence of mitochondria with different OXPHOS capacities or degrees of specialization for OXPHOS⁴⁰. Our data established a variation in MRC both between GM and WM reference samples and across anatomical structures in the coronal section (Fig. 2d). Thus, beyond the expected variation in mitochondrial density between GM and WM, these results reveal the extent to which maximal respiratory capacity, on a per-mitochondrion basis, varies across the human brain.

Brain-area-specific mitochondria

We next registered the coordinates of each voxel to the standard Montreal Neurological Institute (MNI) space (<https://www.bic.mni.mcgill.ca/ServicesAtlases/ICBM152NLin2009>), the most widely used reference neuroanatomical space for MRI research. Each voxel was manually annotated as GM ($n = 325$), WM ($n = 132$) or mixed ($n = 176$) by an anatomy expert (M.T.d.S.) and labelled with its stereotaxic location (Extended Data Fig. 6). The anatomical identity of the voxels was further confirmed by staining adjacent thin tissue sections for Nissl substance, which labels neurons and glia, and for the neuronal nuclear marker NeuN, which labels neurons only (Extended Data Fig. 1h,i).

Projecting all annotated voxels with the full set of mitochondrial parameters in a uniform manifold approximation and projection (UMAP) space produced clusters identified visually that mapped clearly onto gross voxel composition (GM and WM; Fig. 2e). Conversely, when UMAP clusters were used to predict the origin of the voxels, they mapped to GM and WM voxel locations with 82% and 64% accuracy, respectively (chance level = 51% (GM) and 21% (WM); Extended Data Fig. 7a). The remaining voxels were assigned to the mixed category containing both WM and GM tissue, which made the misclassification rate 1–5%. Furthermore, GM and WM voxels exhibited large differences in all mitochondrial features ($g = 1.8\text{--}2.6$; Fig. 2f). Compared with GM, WM contained significantly less mitochondrial mass and total OXPHOS capacity (MitoD and TRC), but WM voxels exhibited a disproportionately low TRC relative to MitoD (Extended Data Fig. 7b). Consequently, the MRC, which reflects mitochondria specialization for energy transformation on a per-mitochondrion basis, was lowest in the WM voxels (Fig. 2f).

A more detailed analysis that focused on GM voxels resulted in four UMAP clusters with distinct mitochondrial activity profiles (Fig. 2g–i and Extended Data Fig. 7c). Notably, although cortical and subcortical areas had similar MitoD values (Fig. 2j,k), cortical GM areas exhibited higher TRC ($P < 0.01$, t -test; $g = 1.1$) and MRC ($P < 0.01$; $g = 1.4$) values than the subcortex. An exception was the putamen, a subcortical structure with the highest TRC and MitoD values. This result could be attributed to the high density of terminal synapses and neurites and

axonal projections in this area⁴², including large axonal arborubs from the tonically active substantia nigra pars compacta dopaminergic neurons⁴³. Moreover, the putamen had the highest nuclear DNA content and therefore numerous cell bodies. The putamen has also undergone an evolutionary exaptation, which may account for this difference⁴⁴. Conversely, we observed high cell density and low MRC in the internal and external pallidum and among several WM regions.

In comparative anatomy, the presence or absence of structures across species enable the phylogenetic classification of major human brain structures^{45–48}. The brainstem, pallidal and striatal areas are uniformly acknowledged as the oldest, whereas cortical areas represent the most recent evolutionary development. Our results showed that both the TRC and MRC correlated strongly with the estimated phylogenetic age of brain regions. Mitochondria in brain regions that emerged later in the evolutionary timeline—moving from reptiles to mammals and further to primates and humans—exhibited higher MRC values ($\rho = 0.72\text{--}0.75$, $P > 0.01$; Fig. 2l). This enzymatic specialization aligns with the hypothesis that an evolutionary gradient exists with an increased metabolic demand¹². Our data show that this demand is met by a specialized mitochondrial phenotype (mitotype) with high OXPHOS capacity per mitochondrion.

Cell-type-specific mitochondria

Specialized mitotypes map either to specific brain areas⁵ or to specific cell types^{6,49}, which differ in their abundance among different brain areas (WM versus GM; cortical versus subcortical differ in their cyto-architecture^{35,50,51}). To profile cell-type-specific molecular mitotypes across the human brain, we performed single-nucleus RNA sequencing (snRNA-seq) on individual nuclei recovered from voxel homogenates prepared for the mitochondrial enzymatic measurements presented above. The lysis-oriented chemistry and aggressive mechanical disruption required for mitochondrial enzyme assays contrast with the gentler approaches typically required to generate high-quality preparations for snRNA-seq⁵². As such, this limitation of our approach should be corrected in future studies seeking to establish cell-type-specific mitotypes.

We selected individual voxels from four areas: the cortex (that is, the middle temporal gyrus (MTg)), the hippocampus, the putamen and the corpus callosum (that is, WM), thereby covering a range of brain areas with wide differences in cell-type composition. Histochemical staining of neurons and glia (Nissl) or neurons only (NeuN) on 50- μm -thick brain sections confirmed the expected cellular identity of each voxel (Fig. 3a and Extended Data Fig. 8). After applying stringent data-cleaning and quality-control thresholds, we computationally recovered a total of 32,515 nuclei (8,945 for the MTg, 7,044 for the hippocampus, 6,176 for the putamen and 10,350 for the corpus callosum) that could be categorized into 9 broad cell types (Fig. 3b). This result confirmed the expected differences in cell composition across each stereotactically defined voxel (Fig. 3c).

Mitochondrial specialization arises from the regulated expression of about 1,136 mitochondrial genes or proteins, as validated by the MitoCarta3.0 inventory¹⁹. Using pseudo-bulk transcriptomes (that is, mimicking bulk RNA-seq), we recovered 1,118 nuclear-encoded and mtDNA-encoded mitochondrial genes and calculated OXPHOS scores for each voxel and OXPHOS subunit⁵. As for our molecular and biochemical results, the WM voxel exhibited lower mtDNA-encoded genes than GM voxels (Fig. 3d; log fold change < -1.5 , adjusted $P < 0.001$). Overall, although data from only four voxels were insufficient to draw definitive conclusions, the relative gene expression of subunits of the OXPHOS complex were proportional to the measured enzymatic activities of CI, CII and CIV in the putamen, the hippocampus and WM (Fig. 3d). This result provides partial convergent evidence for the observed enzymatic data; however, additional validation in larger datasets is required. One exception was a low expression of CI and CII subunits

Article

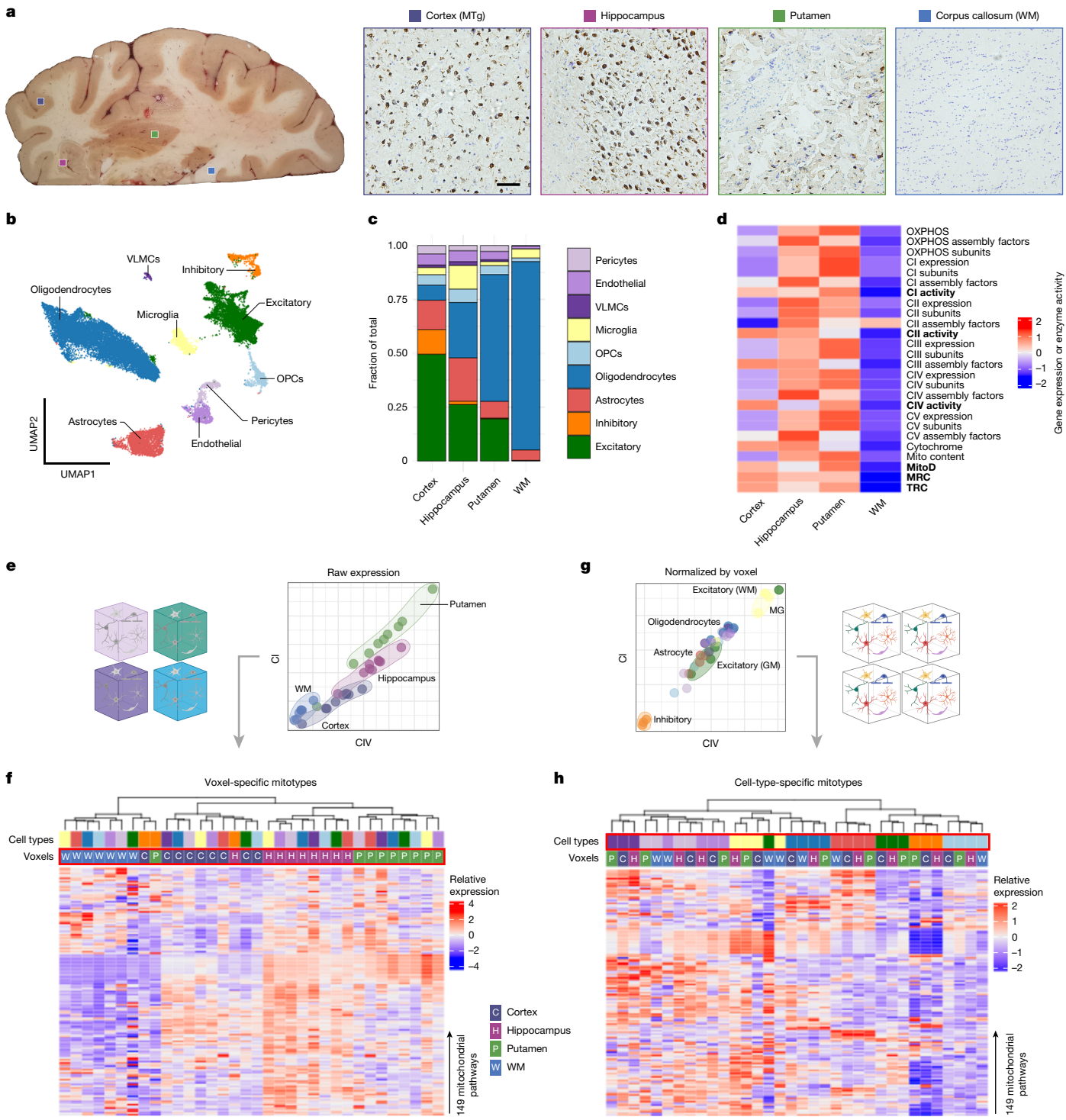


Fig. 3 | snRNA-seq analysis of selected voxels. **a**, Left, location of voxels selected for snRNA-seq analysis and their histological evaluation. Right, thin brain slices were stained with Nissl (blue, all nuclei) and immunolabelled for NeuN (brown, neuronal cells). Scale bar, 100 µm. **b**, UMAP plot of cell clusters identified by snRNA-seq analysis of four voxels, showing nine major cell types. OPCs, oligodendrocyte precursor cells; VLMCs, vascular leptomeningeal cells. **c**, Cell-type proportions in each of the four voxels. **d**, Heatmap of OXPHOS pathway gene expression scores of each voxel (pseudobulk expression per sample), together with the measurements of activity (highlighted in bold). **e**, Correlations of raw expression levels between C1 and CIV. Each data point represents the pseudobulk expression of OXPHOS subunits in each voxel and

f, Heatmap of expression scores of 149 mitochondrial pathways (Supplementary Data 1). Each column represents raw expression scores in a voxel and cell type, colour coded in the first two rows (same colours as in **a** for voxels and **c** for cell types). Note the clustering of the samples by their voxel type. **g**, Correlations between C1 and CIV expression after z-score normalization of expression levels in each voxel type to account for region-specific differences. Each data point is colour coded by its cell type. **h**, Heatmap of mitochondrial pathway expression scores in voxels and cell types after expression was normalized in each voxel. The clustering of samples by their cell type is now obvious. Parts **e** and **g** created in BioRender. Mosharov, E. (2025) <https://BioRender.com/z524941>.

in the cortex that was not reflected in the measurements of enzyme activity. The putamen had the highest scores for both OXPHOS expression and enzyme activity, despite the low abundance of recovered neurons. This result suggests that either the recovered nuclei do not faithfully represent the cell types present in the brain areas or there are region-specific drivers of enzymatic mitotypes independent of cell-type composition, such as local activity or functional connectivity patterns.

To investigate how different cell types may underlie mitotypes by brain region, we compared mRNA abundance of two OXPHOS complexes (CI and CIV) for matching cell types in each of the four voxels. The raw transcriptional profiles of OXPHOS complexes clustered by voxel rather than cell type (Fig. 3e and Supplementary Data 1). This finding indicated that the major driver of the differences in OXPHOS transcriptome for each cell type is the brain region in which it resides. We then extended this analysis to 149 mitochondrial pathways (MitoCarta3.0), which comprise composite multigene scores that de-emphasize the influence of individual genes to create more stable estimates of functionally relevant mitotype specialization. Again, we found that transcriptional profiles were more similar between different cell types from the same brain region rather than between similar cell types from different regions (Fig. 3f). Thus, most of the variance in brain mitotypes is attributable to regional variations.

Notably, removal of the voxel-to-voxel variation in the overall expression levels by z scoring mRNA levels in each voxel rather than across the entire dataset revealed cell-type-specific mitotypes (Fig. 3g). For instance, relative to other cell types, inhibitory neurons had the lowest expression of OXPHOS complexes, whereas endothelial cells showed the highest expression. Similar robust clustering by cell type rather than voxel location was observed when all mitochondrial gene-expression profiles were normalized for each sample (Fig. 3h).

Overall, our single-nucleus transcriptome analyses indicated that although mitotype differences between human brain cell types exist and are conserved across the brain regions examined, global drivers of mitochondrial gene expression that influence all cell types across brain regions drive the most significant mitochondrial variation. This result is consistent with a topological understanding of brain functional organization⁵³.

Mitochondria and neuroimaging modalities

We next asked whether mitotypes may be reflected in standard neuroimaging modalities, including T1 and T2 MRI, BOLD fMRI and diffusion-weighted images from hundreds of individuals ($n = 1,870$ multimodal brain MRI scans from healthy adults aged 18–35 years)¹¹ (Extended Data Table 1). Such correlations would enable us to predict mitochondrial features using neuroimaging data. Our goal was to extend the map of mitochondrial OXPHOS capacity to the entire brain and to eventually use neuroimaging data to derive personalized MRI-based maps of mitotypes.

As described above, each voxel from our coronal section was registered to its corresponding resolution-matched voxel in the standard MNI brain atlas. Accurate mapping of each voxel was manually verified. Samples with a sum of GM and WM probabilities less than 70% were discarded to avoid partial volume effect contamination. The remaining 539 voxels with all mitochondrial features measured and correctly mapped to the stereotaxic space were randomly divided into 2 groups to train the model (80%, or 431 of voxels) and to test the model (20%, 107 voxels) (Extended Data Fig. 9a and Supplementary Data 2). Each mitochondrial feature (CI, CII, CIV, MitoD, TRC and MRC) was regressed onto 22 structural, functional and diffusion-based neuroimaging metrics using a stepwise linear regression model⁵⁴. Some parameters, such as the orientation dispersion index, a proxy for neurite complexity⁵⁵, were positively associated with all mitochondrial metrics (Extended Data Table 1). By contrast, while some MRI metrics showed

no significant relationship with mitochondrial OXPHOS, others were significantly related, displaying either a positive or negative regression coefficient depending on the specific features (Extended Data Table 1).

Using linear equations from the regression model, the prediction accuracy of mitochondrial features in out-of-sample voxels (20% of samples) based solely on MRI metrics ranged between $R^2 = 0.26$ and 0.36 (all $P < 0.0001$; Fig. 4a). By comparison, prediction of the null model with scrambled voxels returned accuracies of $<0.1\%$ ($P > 0.7$; Extended Data Fig. 9c). When the test samples were collapsed into their respective brain regions, the observed-to-expected correlations were two to three times stronger, which emphasized the robust regional variation in mitotypes (Fig. 4b). The out-of-sample accuracy of the model was also tested by using the MRI-based model to predict the mitochondrial markers in the occipital lobe from the same donor brain (not used in the prediction model). When compared across the six mitochondrial features, the model produced significant agreement between observed and predicted values ($r = 0.75$; Table 1 and Fig. 4h). The predicted and observed mitochondrial feature maps, projected on the coronal slice that was biochemically examined, showed substantial similarities (Extended Data Fig. 9d). This result provided additional support for the accuracy of the model. Further exploration of nonlinear transformations of the variables did not significantly enhance out-of-sample prediction accuracy (see Methods for details).

Encouraged by the ability of the model to predict out-of-sample mitochondria characteristics on the basis of MRI features, we next expanded it to calculate mitochondria density and OXPHOS activities at the scale of the whole brain. The resulting cortical and WM track maps revealed regional specialization for all mitochondrial features ($n = 1,827,243$ voxels at 1 mm^3 resolution; Fig. 4c–e). Mitochondrial specialization was particularly high for the MRC and the OXPHOS enzymes and comparatively more modest for the mitochondrial content (MitoD). This result suggests that different brain areas are expected to vary less in their mitochondrial content and substantially more in their mitochondrial specialization for ATP synthesis (that is, MRC). Accordingly, our neuroimaging-based estimates of MRC across the brain showed a significant correlation with maps that estimated brain evolution (evolutionary expansion⁵⁶ and evolutionary variability⁵⁷) (Extended Data Fig. 10), a result consistent with the region-based analysis shown in Fig. 2l.

Finally, we generated a UMAP representation of the predicted brain-wide mitotypes (anatomical annotation confidence $>80\%$), which further confirmed the marked contrast between GM and WM regions across all mitochondrial features (Fig. 4f,g). Again, the magnitude of gradients was particularly large for CI, CII and CIV activities and the MRC, which reflected the predicted regional specialization of mitochondria. Furthermore, the multivariate UMAP space mapped relatively well with the anatomical and stereotaxic coordinates of cortical and subcortical GM regions and WM tracts, including regions not presented in our initial brain section. Thus, these results establish an approach to use standard MRI parameters to predict biochemical and molecular mitochondrial profiles across the human brain.

Discussion

We generated an atlas of mitochondrial content, enzymatic OXPHOS activities and specialization across the human brain, which established the diversity of mitotypes at a resolution comparable to MRI. Enabled by a method to physically voxelize frozen human brain tissue, our results revealed roles for both regional and cell-type-level factors that contribute to the molecular mitotype diversity observed throughout the human brain. Notably, the distinct mitotypes between the GM and WM align with well-known regional variation in metabolic requirements across brain tissue^{5–10,12–15}. This finding highlights a possible predisposition for mitochondrial disorders to affect cortical structures, such as stroke-like episodes that selectively affect and spread across

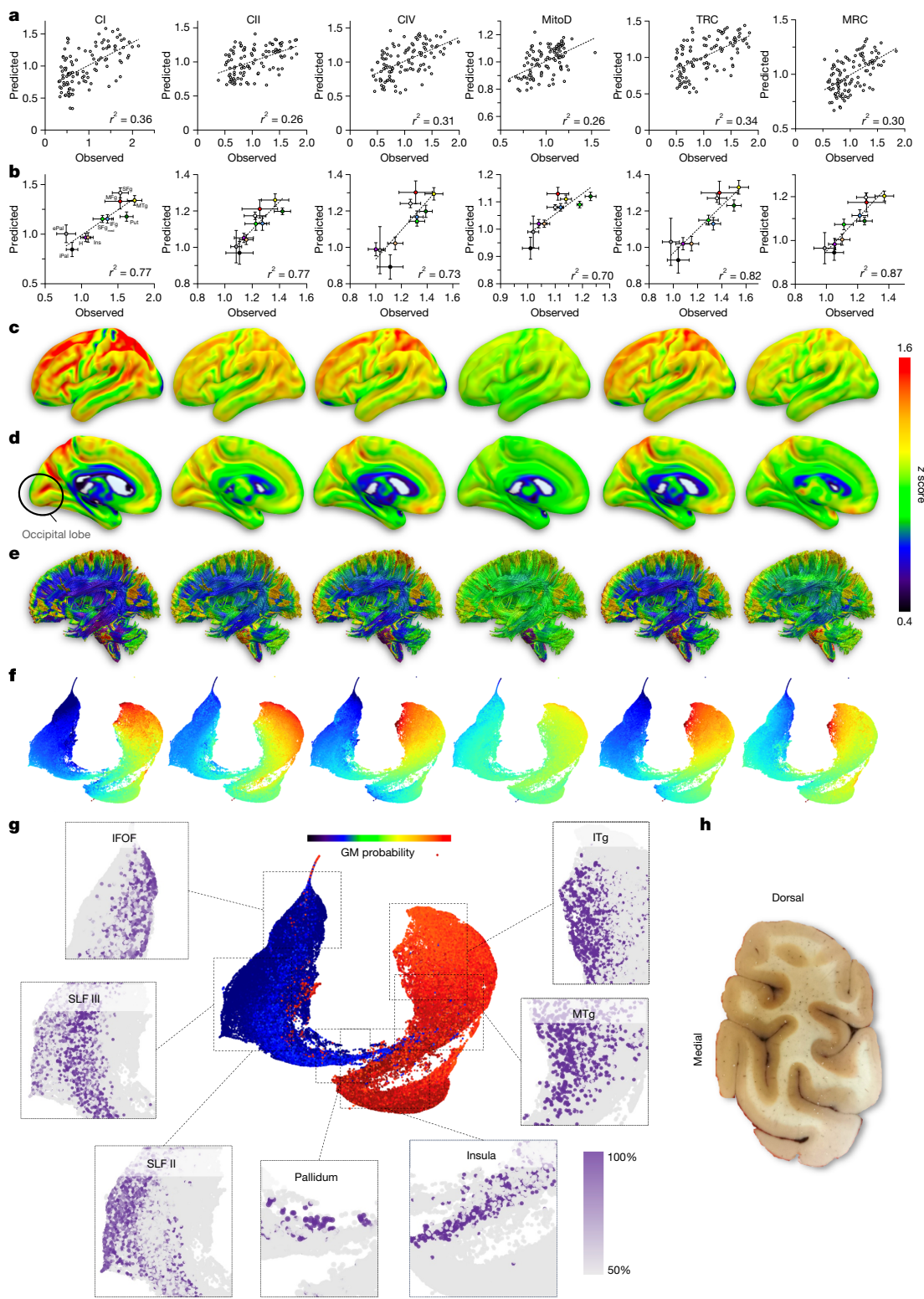


Fig. 4 | Projected mitochondrial activities of the entire brain. **a**, Scatterplots of 20% out-of-sample prediction of mitochondrial profiles (Extended Data Fig. 9). **b**, Correlations between observed and predicted mitochondrial features for brain areas rather than individual samples. Both learning and testing samples were used. $n = 5$ voxels (ePal and iPal), 7 voxels (MTg), 9 voxels (MFg), 11 voxels (IFG_{med}) 15 voxels (H, Put and SFG), 27 voxels (Ins) and 33 voxels (IFg). Slopes of all linear regressions in **a** and **b** are different from zero ($P < 0.0001$; Pearson's r^2 is shown on each graph). **c–e**, Prediction of whole brain values for the lateral (**c**) and the medial (**d**) surfaces and the WM connections (**e**, lateral view). Three-dimensional maps are available at <https://neurovault.org/neurovault.collection:16418>. **f**, UMAP embedding of the whole brain at

1 mm³ resolution, colours indicate mitochondrial activity profiles. **g**, UMAP plot of the whole brain with colours indicating the probability of each point being located in the WM or GM. Insets show probabilities of voxels being in specific WM (inferior fronto-occipital fasciculus (IFOF), superior longitudinal fasciculus (SLF)) or GM (pallidum, insula, MTg, inferior temporal gyrus (ITg)) brain structures ($P < 0.0001$, Bonferroni-corrected for multiple comparisons). **h**, Image of the occipital lobe brain slab before milling. Summary of mitochondrial features in the pooled GM occipital lobe samples used as loading controls (Extended Data Fig. 2d) and predicted values generated by averaging MRI-based model predicted mitochondrial metrics in ten randomly selected occipital lobe voxels in the MNI space are shown in Table 1.

Table 1 | Correlation between observed and predicted mitochondrial parameters for an out-of-sample (occipital lobe) brain area

| Feature | Observed | Predicted |
|---------|-----------|-----------|
| CI | 1.43±0.27 | 1.41±0.26 |
| CII | 1.25±0.16 | 1.35±0.14 |
| CIV | 1.44±0.17 | 1.31±0.24 |
| MitoD | 1.17±0.02 | 1.15±0.07 |
| TRC | 1.39±0.15 | 1.32±0.18 |
| MRC | 1.22±0.13 | 1.23±0.12 |

Values are means±s.d. Observed and predicted datasets were not different by two-way ANOVA ($F_{1,144}=0.69$, $P=0.41$; Pearson's $r=0.75$).

cortical areas with a topology not restricted to arterial vascular territories⁵⁸. These data could also implicate the existence of compensatory mechanisms in the WM that may mitigate cortical deficits in diseases like stroke⁵⁹.

The alignment of mitochondria molecularly specialized for energy transformation (high MRC) with evolutionary patterns sheds light on the underlying subcellular bioenergetic infrastructure evolved to sustain the increased energy costs specific to humans⁶⁰, particularly in regions associated with human-specific cognitive functions¹². Recent work has highlighted how cortical brain regions recruited to perform executive functions express high levels of cell surface receptors for neuromodulators and depend highly on glucose consumption¹². This dependence also agrees with the neuropsychological vulnerability of evolutionary advanced cognitive functions among individuals with inherited mitochondrial diseases⁶¹, and with the cognitive domains affected by the age-related accumulation of defects on the mitochondrial genome^{62–64}.

Rapidly accumulating evidence showing that neuropsychiatric and age-related brain disorders involve mitochondrial alterations has motivated basic and clinical research communities to image mitochondrial biology in the living brain. In parallel with PET-based metabolic imaging, our model that predicts molecular mitotypes across the brain using common neuroimaging modalities^{11,65} meets this need and opens the door to new questions that bridge the scale gap between cognitive neuroscience and mitochondrial biology.

However, limitations of the current study should be noted. Our prediction model is based on neuroimaging data from a group template and is subject to inter-individual anatomical variability. The reliance on a single neurotypical human brain sample, akin to other whole-brain microscopy initiatives^{35–37}, underscores the necessity for additional post-mortem datasets to determine the generalizability of our neuroimaging model to other healthy and pathological samples from individuals of different ages and sexes. A generalizable model would mean that mitochondrial assays in a small tissue sample (or samples) precisely mapped to the anatomy of the human brain could generate predictions and hypotheses for the whole brain. The scale of this task is technically challenging. Nevertheless, mapping inter-individual differences in the subcellular energetic architecture—in specific cell types and among different brain regions—is crucial to advance our understanding of the energetic infrastructure that supports and possibly instructs large-scale brain activity dynamics in different brains⁶⁶.

In summary, our physical voxelization approach and molecular phenotyping study established the spatial distribution of mitochondrial diversity in the human brain, and revealed marked disparities between GM and WM and among key cerebral regions. This work not only revealed a gradient that parallels the phylogenetic development of the brain but also provided a scalable approach to deciphering the mitochondrial underpinnings of human brain evolution, healthy

development and disease. Bridging the scale gap from organelle to whole-brain biology and neuroimaging lays the foundation to understanding the mitochondrial and energetic basis of brain function and dysfunction across a variety of contexts.

Online content

Any methods, additional references, Nature Portfolio reporting summaries, source data, extended data, supplementary information, acknowledgements, peer review information; details of author contributions and competing interests; and statements of data and code availability are available at <https://doi.org/10.1038/s41586-025-08740-6>.

- Shulman, R. G., Hyder, F. & Rothman, D. L. Baseline brain energy supports the state of consciousness. *Proc. Natl Acad. Sci. USA* **106**, 11096–11101 (2009).
- Zhang, D. & Raichle, M. E. Disease and the brain's dark energy. *Nat. Rev. Neurol.* **6**, 15–28 (2010).
- Minhas, P. S. et al. Restoring metabolism of myeloid cells reverses cognitive decline in ageing. *Nature* **590**, 122–128 (2021).
- Daniels, T. E., Olsen, E. M. & Tyrka, A. R. Stress and psychiatric disorders: the role of mitochondria. *Annu. Rev. Clin. Psychol.* **16**, 165–186 (2020).
- Rosenberg, A. M. et al. Brain mitochondrial diversity and network organization predict anxiety-like behavior in male mice. *Nat. Commun.* **14**, 4726 (2023).
- Fecher, C. et al. Cell-type-specific profiling of brain mitochondria reveals functional and molecular diversity. *Nat. Neurosci.* **22**, 1731–1742 (2019).
- Tomasini, D., Wang, G.-J. & Volkow, N. D. Energetic cost of brain functional connectivity. *Proc. Natl Acad. Sci. USA* **110**, 13642–13647 (2013).
- He, X. et al. Uncovering the biological basis of control energy: structural and metabolic correlates of energy inefficiency in temporal lobe epilepsy. *Sci. Adv.* **8**, eabn2293 (2022).
- Yu, Y. et al. A 3D atlas of functional human brain energetic connectome based on neuropil distribution. *Cereb. Cortex* **33**, 3996–4012 (2023).
- Blazey, T. et al. Quantitative positron emission tomography reveals regional differences in aerobic glycolysis within the human brain. *J. Cereb. Blood Flow Metab.* **39**, 2096–2102 (2019).
- Tsuchida, A. et al. The MRI-Share database: brain imaging in a cross-sectional cohort of 1870 university students. *Brain Struct. Funct.* **226**, 2057–2085 (2021).
- Castrillon, G. et al. An energy costly architecture of neuromodulators for human brain evolution and cognition. *Sci. Adv.* **9**, eadi7632 (2023).
- Cui, Z. et al. Optimization of energy state transition trajectory supports the development of executive function during youth. *eLife* **9**, e53060 (2020).
- Pinotsis, D. A., Fridman, G. & Miller, E. K. Cytoelectric coupling: electric fields sculpt neural activity and 'tune' the brain's infrastructure. *Prog. Neurobiol.* **226**, 102465 (2023).
- Strasser, A. et al. Glutamine-to-glutamate ratio in the nucleus accumbens predicts effort-based motivated performance in humans. *Neuropsychopharmacology* **45**, 2048–2057 (2020).
- Padamsey, Z. & Rochefort, N. L. Paying the brain's energy bill. *Curr. Opin. Neurobiol.* **78**, 102668 (2023).
- Pekkurnaz, G. & Wang, X. Mitochondrial heterogeneity and homeostasis through the lens of a neuron. *Nat. Metab.* **4**, 802–812 (2022).
- Monzal, A. S., Enriquez, J. A. & Picard, M. Multifaceted mitochondria: moving mitochondrial science beyond function and dysfunction. *Nat. Metab.* **5**, 546–562 (2023).
- Rath, S. et al. MitoCart3.0: an updated mitochondrial proteome now with sub-organelle localization and pathway annotations. *Nucleic Acids Res.* **49**, D1541–D1547 (2021).
- Picard, M. & Shirihai, O. S. Mitochondrial signal transduction. *Cell Metab.* **34**, 1620–1653 (2022).
- Styr, B. et al. Mitochondrial regulation of the hippocampal firing rate set point and seizure susceptibility. *Neuron* **102**, 1009–1024 (2019).
- Kwon, S.-K. et al. LKB1 regulates mitochondria-dependent presynaptic calcium clearance and neurotransmitter release properties at excitatory synapses along cortical axons. *PLoS Biol.* **14**, e1002516 (2016).
- Lin, M.-M., Liu, N., Qin, Z.-H. & Wang, Y. Mitochondrial-derived damage-associated molecular patterns amplify neuroinflammation in neurodegenerative diseases. *Acta Pharmacol. Sin.* **43**, 2439–2447 (2022).
- Joshi, A. U. et al. Fragmented mitochondria released from microglia trigger A1 astrocytic response and propagate inflammatory neurodegeneration. *Nat. Neurosci.* **22**, 1635–1648 (2019).
- Hara, Y. et al. Presynaptic mitochondrial morphology in monkey prefrontal cortex correlates with working memory and is improved with estrogen treatment. *Proc. Natl Acad. Sci. USA* **111**, 486–491 (2014).
- Sharpley, M. S. et al. Heteroplasmy of mouse mtDNA is genetically unstable and results in altered behavior and cognition. *Cell* **151**, 333–343 (2012).
- Hollis, F. et al. Mitochondrial function in the brain links anxiety with social subordination. *Proc. Natl Acad. Sci. USA* **112**, 15486–15491 (2015).
- Gebara, E. et al. Mitofusin-2 in the nucleus accumbens regulates anxiety and depression-like behaviors through mitochondrial and neuronal actions. *Biol. Psychiatry* **89**, 1033–1044 (2021).
- Huang, S. C. et al. Noninvasive determination of local cerebral metabolic rate of glucose in man. *Am. J. Physiol.* **238**, E69–E82 (1980).
- Theriault, J. E. et al. A functional account of stimulation-based aerobic glycolysis and its role in interpreting BOLD signal intensity increases in neuroimaging experiments. *Neurosci. Biobehav. Rev.* **153**, 105373 (2023).

31. van Zijl, P. C. M. & Yadav, N. N. Chemical exchange saturation transfer (CEST): what is in a name and what isn't? *Magn. Reson. Med.* **65**, 927–948 (2011).
32. Brennan, B. P., Rauch, S. L., Jensen, J. E. & Pope, H. G. A critical review of magnetic resonance spectroscopy studies of obsessive-compulsive disorder. *Biol. Psychiatry* **73**, 24–31 (2013).
33. Goyal, M. S. et al. Loss of brain aerobic glycolysis in normal human aging. *Cell Metab.* **26**, 353–360 (2017).
34. Rae, C. D. et al. Brain energy metabolism: a roadmap for future research. *J. Neurochem.* **168**, 910–954 (2024).
35. Amunts, K. et al. BigBrain: an ultrahigh-resolution 3D human brain model. *Science* **340**, 1472–1475 (2013).
36. Howard, A. F. D. et al. An open resource combining multi-contrast MRI and microscopy in the macaque brain. *Nat. Commun.* **14**, 4320 (2023).
37. Alkemade, A. et al. A unified 3D map of microscopic architecture and MRI of the human brain. *Sci. Adv.* **8**, eabj7892 (2022).
38. Osto, C. et al. Measuring mitochondrial respiration in previously frozen biological samples. *Curr. Protoc. Cell Biol.* **89**, e116 (2020).
39. Acin-Perez, R. et al. A novel approach to measure mitochondrial respiration in frozen biological samples. *EMBO J.* **39**, e104073 (2020).
40. Picard, M. et al. A mitochondrial health index sensitive to mood and caregiving stress. *Biol. Psychiatry* **84**, 9–17 (2018).
41. Finnegan, J. M. et al. Vesicular quantal size measured by amperometry at chromaffin, mast, pheochromocytoma, and pancreatic β -cells. *J. Neurochem.* **66**, 1914–1923 (1996).
42. Haber, S. N. Neurotransmitters in the human and nonhuman primate basal ganglia. *Hum. Neurobiol.* **5**, 159–168 (1986).
43. Bolam, J. P. & Pissadaki, E. K. Living on the edge with too many mouths to feed: why dopamine neurons die. *Mov. Disord.* **27**, 1478–1483 (2012).
44. Grillner, S. & Robertson, B. The basal ganglia over 500 million years. *Curr. Biol.* **26**, R1088–R1100 (2016).
45. Darwin, C. *On the Origin of Species by Means of Natural Selection, or the Preservation of Favoured Races in the Struggle for Life* 1st edn (John Murray, 1859).
46. de Sousa, A. A. et al. From fossils to mind. *Commun. Biol.* **6**, 636 (2023).
47. Friedrich, P. et al. Imaging evolution of the primate brain: the next frontier? *NeuroImage* **228**, 117685 (2021).
48. Pandya, D., Petrides, M. & Cipolloni, P. B. *Cerebral Cortex: Architecture, Connections, and the Dual Origin Concept* (Oxford Univ. Press, 2015).
49. Dükung, T. et al. Ketogenic diet uncovers differential metabolic plasticity of brain cells. *Sci. Adv.* **8**, eabo7639 (2022).
50. Amunts, K., Mohlberg, H., Bludau, S. & Zilles, K. Julich-Brain: a 3D probabilistic atlas of the human brain's cytoarchitecture. *Science* **369**, 988–992 (2020).
51. Tran, M. N. et al. Single-nucleus transcriptome analysis reveals cell-type-specific molecular signatures across reward circuitry in the human brain. *Neuron* **109**, 3088–3103 (2021).
52. Slyper, M. et al. A single-cell and single-nucleus RNA-seq toolbox for fresh and frozen human tumors. *Nat. Med.* **26**, 792–802 (2020).
53. Margulies, D. S. et al. Situating the default-mode network along a principal gradient of macroscale cortical organization. *Proc. Natl. Acad. Sci. USA* **113**, 12574–12579 (2016).
54. Hocking, R. R. A biometrics invited paper. The analysis and selection of variables in linear regression. *Biometrics* **32**, 1–49 (1976).
55. Zhang, H., Schneider, T., Wheeler-Kingshott, C. A. & Alexander, D. C. NODDI: practical in vivo neurite orientation dispersion and density imaging of the human brain. *NeuroImage* **61**, 1000–1016 (2012).
56. Hill, J. et al. Similar patterns of cortical expansion during human development and evolution. *Proc. Natl. Acad. Sci. USA* **107**, 13135–13140 (2010).
57. Croxson, P. L., Forkel, S. J., Cerliani, L. & Thiebaut de Schotten, M. Structural variability across the primate brain: a cross-species comparison. *Cereb. Cortex* **28**, 3829–3841 (2018).
58. Cheng, W., Zhang, Y. & He, L. MRI features of stroke-like episodes in mitochondrial encephalomyopathy with lactic acidosis and stroke-like episodes. *Front. Neurol.* **13**, 843386 (2022).
59. Forkel, S. J. et al. Anatomical predictors of aphasia recovery: a tractography study of bilateral perisylvian language networks. *Brain J. Neurol.* **137**, 2027–2039 (2014).
60. Pontzer, H. et al. Metabolic acceleration and the evolution of human brain size and life history. *Nature* **533**, 390–392 (2016).
61. Moore, H. L., Blain, A. P., Turnbull, D. M. & Gorman, G. S. Systematic review of cognitive deficits in adult mitochondrial disease. *Eur. J. Neurol.* **27**, 3–17 (2020).
62. Klein, H.-U. et al. Characterization of mitochondrial DNA quantity and quality in the human aged and Alzheimer's disease brain. *Mol. Neurodegener.* **16**, 75 (2021).
63. Bose, A. & Beal, M. F. Mitochondrial dysfunction in Parkinson's disease. *J. Neurochem.* **139**, 216–231 (2016).
64. Borsche, M., Pereira, S. L., Klein, C. & Grünewald, A. Mitochondria and Parkinson's disease: clinical, molecular, and translational aspects. *J. Park. Dis.* **11**, 45–60 (2021).
65. Van Essen, D. C. et al. The WU-Minn Human Connectome Project: an overview. *NeuroImage* **80**, 62–79 (2013).
66. Gordon, E. M. et al. Precision functional mapping of individual human brains. *Neuron* **95**, 791–807 (2017).

Publisher's note Springer Nature remains neutral with regard to jurisdictional claims in published maps and institutional affiliations.

Springer Nature or its licensor (e.g. a society or other partner) holds exclusive rights to this article under a publishing agreement with the author(s) or other rightsholder(s); author self-archiving of the accepted manuscript version of this article is solely governed by the terms of such publishing agreement and applicable law.

© The Author(s), under exclusive licence to Springer Nature Limited 2025, corrected publication 2025

Methods

Donor brain selection

Donor brains were collected, evaluated and stored by the Macedonian-NYSPI Brain collection and made available for this study through the Quantitative Brain Biology (Brain QUANT) Institute at the New York State Psychiatric Institute (NYSPI). The study was reviewed and approved by the Institutional Review Board at NYSPI, which determined that it does not constitute research on human participants. The selected brain for study was from a 54-year-old neurotypical man who died from a myocardial infarction (PMI = 8 h, storage time at -80°C for 10 years), had a negative toxicology screen for psychoactive medication, drugs and alcohol, had essentially negative neuropathology and a negative history for neuropsychiatric disorders according to a validated psychological autopsy designed to obtain psychiatric diagnoses through interview of the next of kin⁶⁷. According to his relatives, the donor was right-handed, athletic and did not smoke or drink alcohol. Coronal 2-cm-thick slabs of the right hemisphere were flash-frozen in 1,1,1,2-tetrafluoroethane (R-134a, TGS) and stored at -80°C . For sectioning, we chose a slab for which the anterior side was located at stereotactic MNI coordinate $y = 15.51$ mm posterior of the centre of the anterior commissure (AC), according to the Human Brain Atlas⁶⁸. Physical dimensions of the frozen slab were 130.8 mm (ventral–dorsal) by 61.25 mm (medial–lateral).

Tissue voxelization and sample collection

To perform brain partitioning while maintaining the tissue below -20°C (to ensure that enzymatic activities are minimally affected), we developed a hardware–software platform. The hardware consisted of a CNC router (FoxAlien CNC Router 3018-SE V2) operated in a -25°C freezer room and controlled by a laptop computer in the adjacent room (maintained at 4°C). A software routine in Igor Pro (WaveMetrics) was developed to easily define the parameters to clean and partition a frozen brain slab, generate the G-codes used to control the CNC router, randomize samples and assign them to assay plates, and derandomize the samples after the assays are complete (Supplementary Data 3 and 4).

Using an occipital lobe slab from the selected brain, sectioning parameters (drill diameter, feed rate, spindle speed, among others) were optimized to minimize cutting time while avoiding potential tissue damage due to local heating and maintaining reliable operation during the several hours required for brain cutting. See Extended Data Fig. 1a–c for details on the milling procedure. Once the surface of the brain slab was fully milled, it was placed on dry ice. First, four samples of shavings were collected from the surface above one white (SLF) and three grey (putamen, SFg and MFg) areas. These ‘dust’ samples were processed and quantified together with all other samples. As shown in Extended Data Fig. 2a,b, mitochondrial activities are noticeably affected by local heating and exposure to air.

Next, shavings were gently removed from the surface with a brush, and a pre-chilled scalpel and a pair of forceps were used to collect individual voxels. The scalpel was inserted into the milled cuts by applying light pressure, which released the voxels from the surface of the slab without causing them to pop out. Voxels (703 in total) were then individually picked up with forceps and placed into pre-labelled and pre-weighed 0.5 ml PCR tubes on dry ice. Tubes were then re-weighed to determine the weight of the tissue, transferred to 1.5 ml tubes and stored at -80°C until future processing. To minimize potential batch effects and to blind the experimenter to the origin of the voxel, samples were scrambled using an Igor Pro routine: unique coordinates of each sample on the brain map were substituted with new, randomly generated coordinates on eight 96-well assay plates.

Brain histology

After voxel collection, 0.3 mm of the surface was cleaned and levelled again with a 12.7 mm flat-tip drill bit (Extended Data Fig. 1d–f). The metal plate with the slab was then mounted on a freezing microtome

and 50- μm -thick cryosections were collected onto glass slides for histological evaluation. For anatomical mapping of neurons and glia and for alignment of cell populations with the collected voxels, we performed tissue staining for a neuronal nuclear marker (NeuN) and Nissl as previously described⁶⁹, but with some modifications to adapt the immunostaining process to frozen tissue.

In brief, for NeuN immunohistochemistry, whole hemisphere frozen sections mounted on glass slides were dried at room temperature for 1 h, then fixed in 4% paraformaldehyde in phosphate buffer (0.1 M, pH 7.4) for 3 h at 4°C . After 3 washes in PBS at room temperature, sections were incubated in 3% H₂O₂ and 10% methanol in PBS for 10 min, followed by 3 washes in PBS. After 1 h of pre-incubation in blocking buffer (10% normal horse serum and 0.3% Triton X-100 in PBS), sections were incubated with mouse monoclonal antibodies against NeuN protein (anti-NeuN, clone A60; 1:20,000 dilution; Millipore) overnight at 4°C . Sections were then washed 3 times in PBS and incubated with secondary biotinylated horse antibodies against anti-mouse IgG (1:200 dilution; Vector), followed by avidin–biotinylated peroxidase complex (Vectastain ABC kit elite, Vector) for 2 h at room temperature (1:100 avidin, 1:100 biotin in PBS) and then 5 min in 0.05% diaminobenzidine in 0.1 M sodium acetate.

For Nissl staining with Cresyl violet, after NeuN immunostaining, sections were dried in a desiccator overnight followed by delipidation in increasing percentages of ethanol to 100%, followed by 100% xylene. Then, sections were rehydrated starting from xylene and ending in H₂O, and stained in Cresyl violet (0.1% Cresyl violet acetate, 0.25% glacial acetic acid in H₂O). The staining was differentiated in 90% ethanol and 10% glacial acetic acid. Finally, sections were placed in 100% ethanol followed by 100% xylene before coverslipping.

Sample preparation for mitochondrial assays and snRNA-seq

Homogenization buffer (1 mM EDTA and 50 mM triethanolamine) was added to each sample at 1:50 (g to ml) ratio. Homogenization was performed with 2 tungsten beads using a Tissue Lyser (Qiagen, 85300) run at 30 cycles per s. Samples were homogenized for 1 min, then incubated on ice for 5 min followed by another 1-min cycle of homogenization. The beads were then removed, and samples underwent 3 freeze–thaw cycles, which was determined to result in higher mitochondrial activities. Samples were placed at -80°C for 15 min, then transferred to a room temperature water bath for 4 min. Homogenate from each sample before the freeze–thaw cycles (100–200 μl) was collected for snRNA-seq analysis. The protein concentration was measured in 15 μl of each sample using a Pierce BCA Assay kit (Thermo 23225) per the manufacturer’s instructions. Absorbance at 562 nm was measured on a Tecan Spark plate reader. The sample protein concentration was determined on the basis of the linear regression of an 8-point BCA standard curve (0–20 μg) on a plate-by-plate basis. Samples were stored at -80°C .

Colourimetric assays of mitochondrial enzyme activities

Enzymatic activities were quantified as previously described⁵ with several modifications. In brief, activities of CS, CI, CII and CIV were measured spectrophotometrically in 96-well plates using Spectramax M2 (Spectramax Pro 6, Molecular Devices). Linear slopes reflecting changes in absorbance of the reporter dyes were exported to Microsoft Excel and converted into enzymatic activities using the molar extinction coefficient and dilution factor for each assay. The assays were optimized for the amount of homogenate and substrates to produce stable readings across all samples. Three loading control samples—GM, WM and mixed tissue from the occipital lobe slab of the same brain—were run in duplicate on each plate to ensure that controls would be identical between plates that were run on different days. Thirty voxels of each tissue type were homogenized and pooled to produce technical replicates of the same samples.

Each sample was assayed in three technical replicates (assayed on different plates) plus the same number of negative controls, except

Article

CIV, which requires only one nonspecific activity measure. Overall, 8 plates \times 4 assays \times (3 replicates + 2.5 negative controls) = 176 plates were analysed by colourimetric assays. Samples were thawed in a room temperature water bath for 4 min on the morning of the assays. On each day, 90 samples plus 6 (duplicates of the 3) loading controls were transferred into a 96-deepwell block. A 96-multichannel pipette (VIAFLO 96, 6001) was used to load samples from the block into each of the 96-well triplicate plates and triplicate nonspecific activity plates for each assay. A volume of 10 μ l of homogenate was used to measure activity for each of the enzymes. Plates were stored at 4 °C before the assay. Each day, 22 plates were processed: 6 plates for 3 assays and 4 for the CIV assay.

CS enzymatic activity was determined by measuring the increase in absorbance of 5,5'-dithio-bis-(2-nitrobenzoic acid) (DTNB) at 412 nm at 30 °C in 200 μ l of a reaction buffer containing 200 mM Tris (pH 7.4), 10 mM acetyl-CoA, 10 mM DTNB, 2 mM oxaloacetic acid and 10% w/v Triton X-100. The rate of conversion of DTNB into NTB²⁺ ions indicates the CS enzymatic activity. To measure nonspecific activity, oxaloacetate was removed from the assay mix.

CI activity was determined by measuring a decrease in the absorbance of 2,6-dichloroindophenol (DCIP). Kinetics of changes in DCIP absorbance was measured at 600 nm at 30 °C in 200 μ l of a reaction buffer containing 50 mM potassium phosphate (pH 7.4), 50 mg ml⁻¹ BSA, 20 mM decylubiquinone, 80 mM NADH, 20 mM DCIP, 400 μ M antimycin A and 50 mM potassium cyanide (KCN). Antimycin A and KCN were used to inhibit electron flow through CIII and CIV. The negative control included the CI inhibitors rotenone (500 μ M) and piericidin A (200 μ M).

CII activity was determined by measuring the decrease in absorbance of DCIP at 600 nm at 30 °C in 200 μ l of a reaction buffer containing 50 mM potassium phosphate (pH 7.4), 50 mg ml⁻¹ BSA, 500 μ M rotenone, 500 mM succinate-Tris, 50 mM KCN, 20 mM decylubiquinone, 20 mM DCIP, 50 mM ATP and 400 μ M antimycin A. The negative control included 500 mM sodium-malonate, which inhibits CII.

CIV activity was determined by measuring a decrease in cytochrome c absorbance. The rate of conversion of cytochrome c from a reduced to oxidized state was measured at 550 nm at 30 °C in 200 μ l of reaction buffer containing 100 mM potassium phosphate (pH 7.5), 10% w/v *n*-dodecylmaltoside and 120 μ M of purified reduced cytochrome c. The negative control omitted tissue homogenate to determine the autooxidation of reduced cytochrome c.

For each assay, activity was determined by integrating the optical density (OD) change over a certain time period and then subtracting the nonspecific activity. As some samples had markedly different OD kinetics, two separate integration times were used for each assay, which ensured that samples that had a delayed start or samples that saturated quickly were all accounted for. CS activity was determined by integrating the OD₄₁₂ change over both 150–250 s and 250–500 s and by subtracting the nonspecific activity. CI activity was determined by integrating the OD₆₀₀ change over 50–300 s and 300–600 s and by subtracting the rate of NADH oxidation in the presence of rotenone and piericidin A from the total decrease in absorbance. CII activity was determined by integrating the OD₆₀₀ change over 100–400 s and 400–700 s and by subtracting the absorbance in the presence of malonate from the total decrease in absorbance. CIV activity was determined by integrating the OD₅₅₀ change over 50–150 s and 150–300 s and by subtracting the nonspecific activity from the total decrease in absorbance.

For each assay, the later integration time resulted in more consistent measures for control activities across all plates. Therefore, the activities of the control duplicate samples on each plate were averaged for each of the three controls. Each individual control value was then divided by its duplicate average to determine a correction factor. Correction factors for the duplicate control samples on each plate were then averaged. The average normalization factor across the three controls was then used to normalize the plates. Both the earlier integration time

values and the later integration time values from each sample were then multiplied by the final normalization factor per plate. Nonspecific activity plates were integrated over the full range of the two integration times for each assay (150–500 s for CS, 50–600 s for CI, 100–700 s for CII and 50–300 s for CIV).

Once plates were normalized, each sample had values for both the earlier integration time and the later integration time on all three triplicate plates. The higher value between the two integration times was selected for each plate. Of the three selected values (one from each triplicate plate), the two closest values were selected, and the least similar value was discarded. This resulted in duplicate activity measures for each sample. Mitochondrial enzymatic activities were determined by averaging the duplicates, and the specific activity of each sample was calculated as the total activity minus nonspecific activity (negative control). Nonspecific activity was also calculated by taking the two closest of three measures, except for CIV, which only had one nonspecific activity plate. For CIV, the average nonspecific activity value from each plate was applied to all samples on the plate.

Respirometry assays

For CI, CII and CIV, the basic protocol optimized for previously frozen tissue samples was used as previously described^{38,39}. In brief, the brain homogenate samples were loaded in duplicate onto XF96 Seahorse plates to measure the maximal oxidative capacity of either ETC CI and CIV or CII and CIV on a Seahorse XFe96 instrument. CI and CIV were measured by sequential injection of NADH, antimycin A, TMPD-ascorbate and azide, whereas CII and CIV were measured by injecting succinate-rotenone, antimycin A, TMPD-ascorbate and azide.

Investigators running respirometry assays were blinded to the sample identity until all processing and analyses of the results were complete. Each Seahorse assay plate had eight control wells: the GM, WM and mixed tissue controls that were identical to those used for colourimetric assays, mouse liver mitochondrion (a control for Seahorse and injection function), and a blank control. Samples were loaded at 15 μ l volume and normalized to the protein concentration after data acquisition.

Respirometry data analysis was performed as previously described³⁸. In brief, oxygen consumption rate (OCR) data were extracted from duplicate Seahorse runs using the Agilent Wave Analysis software. CI OCR was calculated as the post-NADH injection OCR minus the post-antimycin A injection OCR. CII OCR was calculated as the post-succinate-rotenone injection OCR minus the post-antimycin A injection OCR. CIV OCR was calculated as the post-TMPD-ascorbate injection OCR minus the post-azide injection OCR.

After values for CI, CII and CIV OCRs were normalized for the protein concentration, traces were analysed for acceptance criteria. Minimal OCR thresholds (<2 s.d. of the average readings from WM samples) were set to 0.5 pmol min⁻¹ μ g⁻¹ for CI and CII, and 1.5 pmol min⁻¹ μ g⁻¹ for CIV. If a sample had CI or CII OCR readings that passed their acceptance criteria, CIV OCR values must exceed 80% of their respective CI OCR or CII OCR reading. Overall, one CIOCR value, one CII OCR value, and two CIV OCR values must pass all acceptance criteria. If a sample did not meet the criteria, the assays were rerun with 25 μ l sample instead of 15 μ l for the initial run. If a sample did not meet the acceptance criteria after the rerun, the data were not included in the final dataset. Overall, out of 703 analysed samples, 70 samples did not pass acceptance criteria for CI activity, 35 for CII activity and 19 for CIV activity.

mtDNA and nDNA

mtDNA and nDNA densities and mtDNACn were measured as previously described⁵ with minor modifications. Homogenates were lysed at 1:10 dilution in lysis buffer (100 mM Tris HCl pH 8.5, 0.5% Tween 20 and 200 g ml⁻¹ proteinase K) for 16 h at 55 °C, 10 min at 95 °C, and then briefly at 4 °C. Plates were then stored at -80 °C and thawed to 4 °C before performing qPCR. The reactions were run in triplicate in 384-well

plates using a liquid handling station (ep-Motion5073, Eppendorf) with 12 µl master mix (TaqMan Universal Master mix fast, Life Technologies, 4444964) and 8 µl of the sample lysate, for a final volume of 20 µl. Each plate contained 90 samples, duplicates of the 3 loading control samples, a negative control (lysis buffer without homogenate) and 8 serial dilutions of HfB1 standard (1:4 dilutions), all of which were measured in triplicate. qPCR reactions with Taqman chemistry were used to simultaneously quantify mitochondrial and nuclear amplicons in the same reactions: *ND1* (mtDNA) and β_2 microglobulin (*B2M*, nDNA). The master mix included 300 nM primers and 100 nM probe: *ND1* forward primer: GAGCGATGGTGAGAGCTAAGGT, reverse primer: CCCTAAACCCGC CACATCT, and the probe: HEX-CCATCACCTCTACATCACCGCCC-3IABkFQ. The *B2M* forward primer: CCAGCAGAGAATGGAAGTC, reverse primer: TCTCTCTCCATTCTCAGTAAGTCACT, and the probe: FAM-ATGTGTCTGGGTTTCATCCATCCGACA-3IABkFQ.

The plates were sealed, briefly centrifuged at 2,000g and subjected to 40× cycles on a QuantStudio 7 flex instrument (Applied Biosystems, 448570) with the following program: 50 °C for 2 min, 95 °C for 20 s, 95 °C for 1 min, and 60 °C for 20 s. To ensure comparable C_t values across plates and assays, thresholds for fluorescence detection for both *ND1* and *B2M* were set to 0.08. Averages, standard deviations and coefficients of variation were computed between qPCR triplicates, and an exclusion cut-off of $C_t > 33$ was applied. Control C_t values were averaged across all plates for each of the three controls, and control values for each plate were then divided by the average to determine a normalization factor. The average normalization factor across the three controls was then used to normalize each plate. The mtDNAcn level was derived from the ΔC_t calculated by subtracting the average mtDNA C_t from the average nDNA C_t , and the mtDNAcn level was calculated by $2^{(\Delta C_t)} \times 2$. For measures of mtDNA density, the C_t value was linearized as $2^{C_t}/(1/10^{-12})$ to derive relative mtDNA abundance per unit of tissue.

MitoTracker Deep Red staining

Measurement of mitochondrial content in previously frozen sample homogenates using MitoTracker Deep Red (MTDR) was performed as previously outlined^{38,39}. In brief, 2.5–80 µg of sample material (based on BCA protein calculations) was loaded into a clear, flat-bottom 96-well plate together with 100 µl MAS buffer containing 1 µM MTDR. After 10 min of incubation at 37 °C, MTDR was removed by centrifuging the plate for 5 min at 2,000g at 4 °C, with no brake for deceleration. The supernatant was carefully removed and samples were resuspended in 100 µl MAS buffer without MTDR. Fluorescence was measured using a Tecan Spark plate reader with 625 nm excitation and 670 nm emission. The relative mitochondrial content was determined after controlling for background fluorescence using a blank well. Note that because of high variability in MTDR assay values, it correlated poorly with CS and mtDNA (Extended Data Fig. 5a) and was not used for the analysis.

Overall number of samples

The following biochemical assays were performed to analyse 703 voxels (including replicates and controls): BCA (8 × 96-well plates, 768 samples); MTDR (8 plates, 768 samples); CI, CII and CS colourimetry (48 plates, 13,608 samples); CIV colourimetry (32 plates, 3,024 samples); CI, CII and CIV respirometry (44 plates, 7,384 samples); and mtDNA and nDNA (24 plates, 2,268 samples). Overall, 164 × 96-well plates (some not fully loaded) and 27,820 individual readouts, including replicates and controls, were analysed. Of the 703 original samples, 633 voxels had all mitochondrial features (CI, CII, CIV, CS and mtDNA) determined, of which 539 voxels mapped accurately to the MNI stereotaxic space.

snRNA-seq

Frozen cell homogenates from four human brain areas (cortex, hippocampus, putamen, and corpus callosum; Fig. 3a) were used for

snRNA-seq. In brief, samples in homogenization buffer (Clontech, 2313A) were thawed on ice, then centrifuged at 500g for 5 min at 4 °C, washed with 4 ml ice-cold EZ prep buffer (Sigma, NUC-101) with 0.2% RNase inhibitor and incubated on ice for 5 min. After centrifugation, the nuclei were washed in 4 ml nuclei suspension buffer (NSB, 1× PBS, 0.01% BSA and 0.1% RNase inhibitor). Isolated nuclei were resuspended in 100–500 µl NSB depending on the pellet size and filtered through a 35 µm cell strainer (Corning, 352235). Nuclei were counted using a Nexcelom Cellometer Vision ×10 objective and an acridine orange and propidium iodide (AO/PI) stain. Next, 20 µl of the AO/PI was pipette mixed with 20 µl of the nuclei suspension and 20 µl was loaded onto a Cellometer cell counting chamber of standard thickness (Nexcelom, CHT4-SD100-002) and counted with the dilution factor set to 2.

The single-nucleus library preparation was constructed using 10x Chromium Next GEM Single Cell 3' Reagent kits v.3.1 (Dual Index) (10x Genomics) according to the manufacturer's protocol. In brief, about 10,000 nuclei were loaded onto a 10x Genomics chromium controller single-cell instrument. Reverse transcription reagents, barcoded gel beads and partitioning oil were mixed with the cells to generate single-cell gel beads in emulsions (GEMs). After reverse transcription and barcoding of the cDNA, GEMs were broken, and pooled fractions were recovered and amplified by PCR. The amplified cDNA was then separated by SPRI size selection into cDNA fractions containing mRNA-derived cDNA (>400 bp), which were further purified through additional rounds of SPRI selection. GEX sequencing libraries were generated from the cDNA fractions, which were analysed and quantified using TapeStation D5000 screening tapes (Agilent) and a Qubit HS DNA quantification kit (Thermo Fisher Scientific). Libraries were pooled and sequenced together on a NovaSeq 6000 with a S4 flow cell (Illumina) using paired-end, dual-index sequencing with 28 cycles for read 1, 10 cycles for i7 index, 10 cycles for i5 index and 90 cycles for read 2. Samples from the four different brain regions were processed for snRNA-seq on the same day to avoid batch effects.

The FASTQ files were processed using the 10x Genomics CellRanger package (v.6.0.0) with human reference data GRCh38-2020-A and a command line option --include-introns. Raw UMI count matrices were further processed using the Cellbender package (v.0.1.0) with command line options of 2,000 expected cells and 20,000 total droplets to remove debris and doublets. Cells with a range of 200–5000 genes, at least 500 counts and less than 11% mtDNA genes were kept, and ribosomal genes were removed. The data were log-normalized, scaled and doublets were removed using DoubletFinder⁷⁰. The four datasets were integrated using Harmony⁷¹. Broad clusters were identified using the human motor cortex dataset from Azimuth⁷² and unspecific clusters were removed. Each dataset was downsampled to 5,000 nuclei for downstream mitochondrial analyses.

For mitochondrial analysis of the snRNA-seq data, we first filtered for all human MitoCarta3.0-annotated mitochondrial genes (MitoCarta3.0)¹⁹. To calculate MitoPathway scores, we used the average expression of all mitochondrial genes of each respective pathway, as annotated in MitoCarta3.0, either for pseudobulk expression of each voxel, or each voxel and cell type. A detailed description of the RNA-seq data analysis can be found in a markdown file in Supplementary Data1, linking each figure and analysis with the respective code.

UMAP for dimension reduction

The UMAP method⁷³ was used to reduce the dimensions of mitochondrial features. UMAP is a nonlinear embedding method that distributes data variability along major axes. It preserves the original pairwise distance between the input data structure over the global distance by projecting data into a newly constructed manifold. The UMAP manifold follows the theoretical framework of Riemannian geometry and algebraic topology. Cells with similar mitochondrial values cluster together in the UMAP morphospace, whereas those with different features are further apart.

Article

Voxel registration to stereotaxic MNI space

The image of the brain slab before milling (Extended Data Fig. 1b) was converted to a Neuroimaging Informatics Technology Initiative (NIfTI) format using a homemade code (Supplementary Data 5). Then, a corresponding grid overlay (Extended Data Fig. 6) was delineated manually onto the converted brain slice using FSL-eyes as part of the FMRIB software library (v.6.0; <https://fsl.fmrib.ox.ac.uk/>) to produce a digital version of the grid saved as an independent NIfTI file. Each voxel of the digital grid was assigned a unique number and labelled as being GM, WM or mixed GM and WM by an expert anatomist (M.T.d.S.). Each voxel was also labelled with an anatomical label derived from the Atlas of Human Brain Connections⁷⁴.

Next, we registered the coronal slice to the MNI space (MNI152 nonlinear 6th generation; <http://www.bic.mni.mcgill.ca>) using affine and elastic deformation provided in the MIPAV (v.10.0) software package (<http://mipav.cit.nih.gov>). After visual inspection for the alignment, the same deformation was applied to the digital grid to obtain a digital grid in the MNI space (Extended Data Fig. 6). The grid was subsequently split and binarized so that each voxel corresponded to one binary NIfTI file. To create a representation of the mitochondrial values in the MNI stereotaxic space, values collected for each sample were attributed to each corresponding NIfTI file that were subsequently summed to produce individual maps of the six mitochondrial parameters (CI, CII, CIV, MitoD, TRC and MRC).

To enable comparisons between these values and neuroimaging data, we used averaged neuroimaging values derived from a sample of 1,870 university students¹¹ and the Human Connectome project⁶⁵. Both datasets were normalized to the MNI152 template space⁷⁵ (Extended Data Table 1). The two databases offered a robust array of neuroimaging metrics with highly correlated values for overlapping data. For example, T1-weighted and fractional anisotropy imaging data from the two datasets correlated with $r = 0.83$ and 0.92, correspondingly, supporting their interchangeable use.

First, mapping of each voxel within the MNI space was manually verified, and samples with a sum of GM and WM probabilities less than 70% (95 samples) were discarded to avoid partial volume effect contamination. The remaining 539 voxels with all mitochondrial features measured and correctly mapped into the stereotaxic space were randomly divided into 80% learning (431 samples) and 20% testing (108 samples) datasets (Extended Data Fig. 9). The predictive model was built by means of six stepwise backward linear regressions with neuroimaging values used as independent variables to predict each of the six mitochondrial values (that is, CI, CII, CIV, MitoD, TRC and MRC) in the learning dataset. In the backward hierarchical linear regression, predictors were eliminated one by one, starting from the least significant. The procedure of elimination continued until the comparison between two consecutive models was not significant. The model produces beta values, which should not be mistaken with Pearson correlation coefficients. Instead, they reflect the regression coefficients, indicating the unique contribution of each predictor to the outcome variable while accounting for the influence of all other variables in the model. To test a null distribution of the values, the same analysis was performed on a randomized version of the same dataset (Extended Data Fig. 9c). Next, the models were applied to the 20% testing dataset to verify the out-of-sample quality of predictions. Then, the model was extended to all the brain voxels of the MNI space at 1 mm³ resolution to produce a whole brain map for each mitochondrial value. Three-dimensional maps of predicted mitochondrial features for the whole human brain are available at <https://identifiers.org/neurovault.collection:16418>.

Additional analyses investigated whether nonlinear relationships, incorporating both exponential and logarithmic models, could improve predictions. The nonlinear model produced better fits between the 80%

observed and predicted mitochondrial features during the training phase. However, when we evaluated the performance of the models on the remaining 20% of out-of-sample predictions (testing phase), the nonlinear transformations did not consistently improve prediction accuracy (paired sample t -test < 1 , $P = 0.68$). Considering these results, the simpler linear model was retained, balancing fit quality and reproducibility.

Evolution and mitochondrial values

To determine whether increased mitochondrial OXPHOS follows a phylogenetic gradient, we used two maps to estimate cortical evolution (Extended Data Fig. 10). The GM variability map has been shown to reflect evolution and individual differences in humans and our closest evolutionary relatives⁵⁷. The second map compares macaque-to-human cortical expansion using a transformation map from Caret⁷⁶. This map was created by aligning 23 landmarks in both species and measuring the geodesic distance between homologous regions (<http://brainvis.wustl.edu/>). The following abbreviations were used: ePal, external pallidum; iPal, internal pallidum; BF, basal forebrain; C, caudate; Put, putamen. Areas present in mammals with some close equivalent in reptiles: Piri, piriform cortex; H, hippocampus. Areas present in mammals but not in reptiles: Ent, entorhinal cortex; Ins, insula; Cing, cingulate cortex. Neocortex in primates: ITg, inferior temporal gyrus; STg, superior temporal gyrus; SFg, superior frontal gyrus. Neocortex in humans: MTg, middle temporal gyrus; MFg, middle frontal gyrus.

Statistical analysis

Data were analysed and graphed using Igor Pro (Wavemetrics; RRID: SCR_000325), Python programming language (RRID: SCR_008394), R Project for statistical computing (RRID: SCR_001905) and Prism 8.0 software (GraphPad Software; RRID: SCR_002798). Datasets with normal distributions were analysed for significance using unpaired Student's two-tailed t -test or ANOVA followed by Tukey's post hoc test. Datasets with non-normal distributions were analysed using the Mann–Whitney U -test or Kruskal–Wallis test with Dunn's adjustment for multiple comparisons. The violin plots are displayed as median \pm quartiles; line graphs and data in the text are expressed as mean \pm s.e.m, unless stated otherwise. Bar and whiskers plots show 25–75 percentile (box), minimal and maximal values (whiskers), the median (horizontal line inside the bar) and the mean (+). The statistical tests used are provided in the figure legends.

Reporting summary

Further information on research design is available in the Nature Portfolio Reporting Summary linked to this article.

Data availability

All data supporting the findings, including the individual mitochondrial features data, correlations coefficients with related PET brain maps and the markdown of the snRNA-seq analysis, are provided as Supplementary Information and are available at <https://neurovault.org/collections/16418/> and are centralized at <http://humanmitobrainmap.bcblab.com>.

Code availability

The computer codes used in this study are provided as Supplementary Information (R Markdown for snRNA-seq data in Supplementary File 1) and are available at <https://neurovault.org/collections/16418>.

67. Kelly, T. M. & Mann, J. J. Validity of DSM-III-R diagnosis by psychological autopsy: a comparison with clinician ante-mortem diagnosis. *Acta Psychiatr. Scand.* **94**, 337–343 (1996).
68. Mai, J. K., Majtanik, M. & Paxinos, G. *Atlas Of The Human Brain* 4th edn (Elsevier, 2016).

69. Boldrini, M. et al. Resilience is associated with larger dentate gyrus, while suicide decedents with major depressive disorder have fewer granule neurons. *Biol. Psychiatry* **85**, 850–862 (2019).
70. Fleming, S. J. et al. Unsupervised removal of systematic background noise from droplet-based single-cell experiments using CellBender. *Nat. Methods* **20**, 1323–1335 (2023).
71. Korsunsky, I. et al. Fast, sensitive and accurate integration of single-cell data with Harmony. *Nat. Methods* **16**, 1289–1296 (2019).
72. Bakken, T. E. et al. Comparative cellular analysis of motor cortex in human, marmoset and mouse. *Nature* **598**, 111–119 (2021).
73. Becht, E. et al. Dimensionality reduction for visualizing single-cell data using UMAP. *Nat. Biotechnol.* **37**, 38–44 (2019).
74. Catani, M. et al. Short frontal lobe connections of the human brain. *Cortex* **48**, 273–291 (2012).
75. Evans, A. C., Janke, A. L., Collins, D. L. & Baillet, S. Brain templates and atlases. *NeuroImage* **62**, 911–922 (2012).
76. Van Essen, D. C. & Dierker, D. L. Surface-based and probabilistic atlases of primate cerebral cortex. *Neuron* **56**, 209–225 (2007).

Acknowledgements This project was supported by NIH grant RF1AG076821 and the Baszucki Brain Research Fund to M.P., a pilot award from the Columbia University Department of Psychiatry to M.P., E.V.M. and M. Boldrini, and the JPB Foundation to E.V.M. and D.S. M.T.d.S. is supported by HORIZON-INFRA-2022 SERV (grant number 101147319) ‘EBRAINS 2.0: A Research Infrastructure to Advance Neuroscience and Brain Health’, by the European Union’s Horizon 2020 research and innovation programme under the European Research Council (ERC) Consolidator grant agreement number 816521 (DISCONNECTOME), the University of Bordeaux’s IdEx ‘Investments for the Future’ program RRI ‘IMPACT’, and the IHU ‘Precision & Global Vascular

Brain Health Institute–VBHI’ funded by the France 2030 initiative (ANR-23-IAHU-0001). P.L.D.J. acknowledges support from the RF1AG057473 grant.

Author contributions E.V.M. and M.P. designed the study and supervised data collection, analyses and interpretation of results. G.B.R., A.J.D., M.B.M., M. Bakalian, J.J.M., M.D.U. and M. Boldrini (Quantitative Brain Biology, Brain QUANT Institute) collected and stored the donor brain, psychiatric autopsy and imaging of thin brain slices. E.V.M. oversaw the hardware and software for physical partitioning (voxelization) of the frozen human brain. A.M.R. and S.B. collected samples and performed biochemical and molecular assays with A.J. C.A.O., L.S. and O.S.S. performed respirometry assays. A.S.M., Y.Z., M.F., V.M. and P.L.D.J. performed snRNA-seq analyses. M.T.d.S. registered the data to MNI coordinates, developed the regression model with MRI parameters and created the brain maps. E.V.M., M.T.d.S., A.S.M. and A.M.R. prepared the figures. E.V.M., M.T.d.S. and M.P. drafted the manuscript. All authors reviewed the final version of the manuscript.

Competing interests The authors declare no competing interests.

Additional information

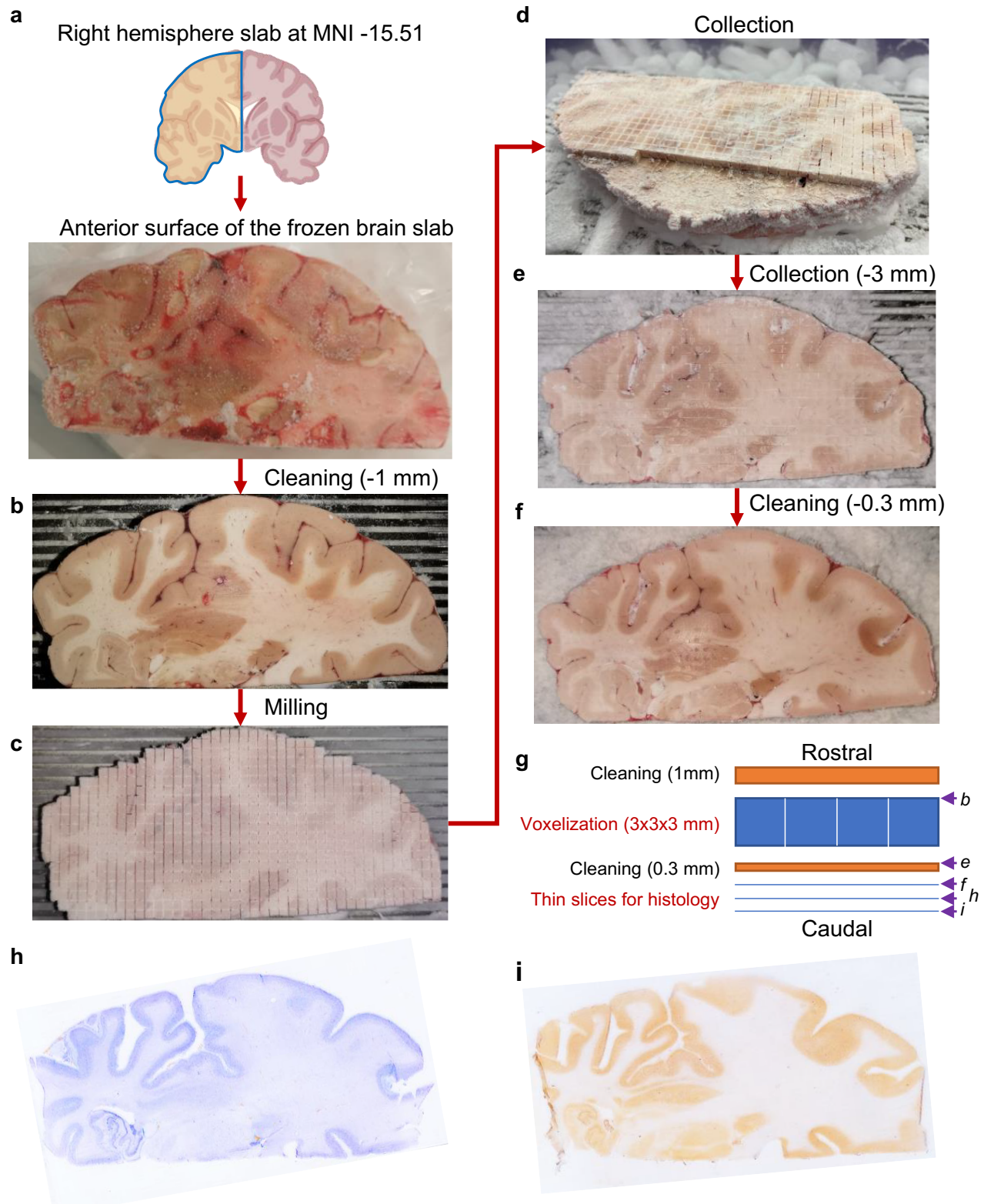
Supplementary information The online version contains supplementary material available at <https://doi.org/10.1038/s41586-025-08740-6>.

Correspondence and requests for materials should be addressed to Michel Thiebaut de Schotten or Martin Picard.

Peer review information *Nature* thanks Vilhelm Bohr, Marco Palombo, Russell Swerdlow and the other, anonymous, reviewer(s) for their contribution to the peer review of this work. Peer reviewer reports are available.

Reprints and permissions information is available at <http://www.nature.com/reprints>.

Article

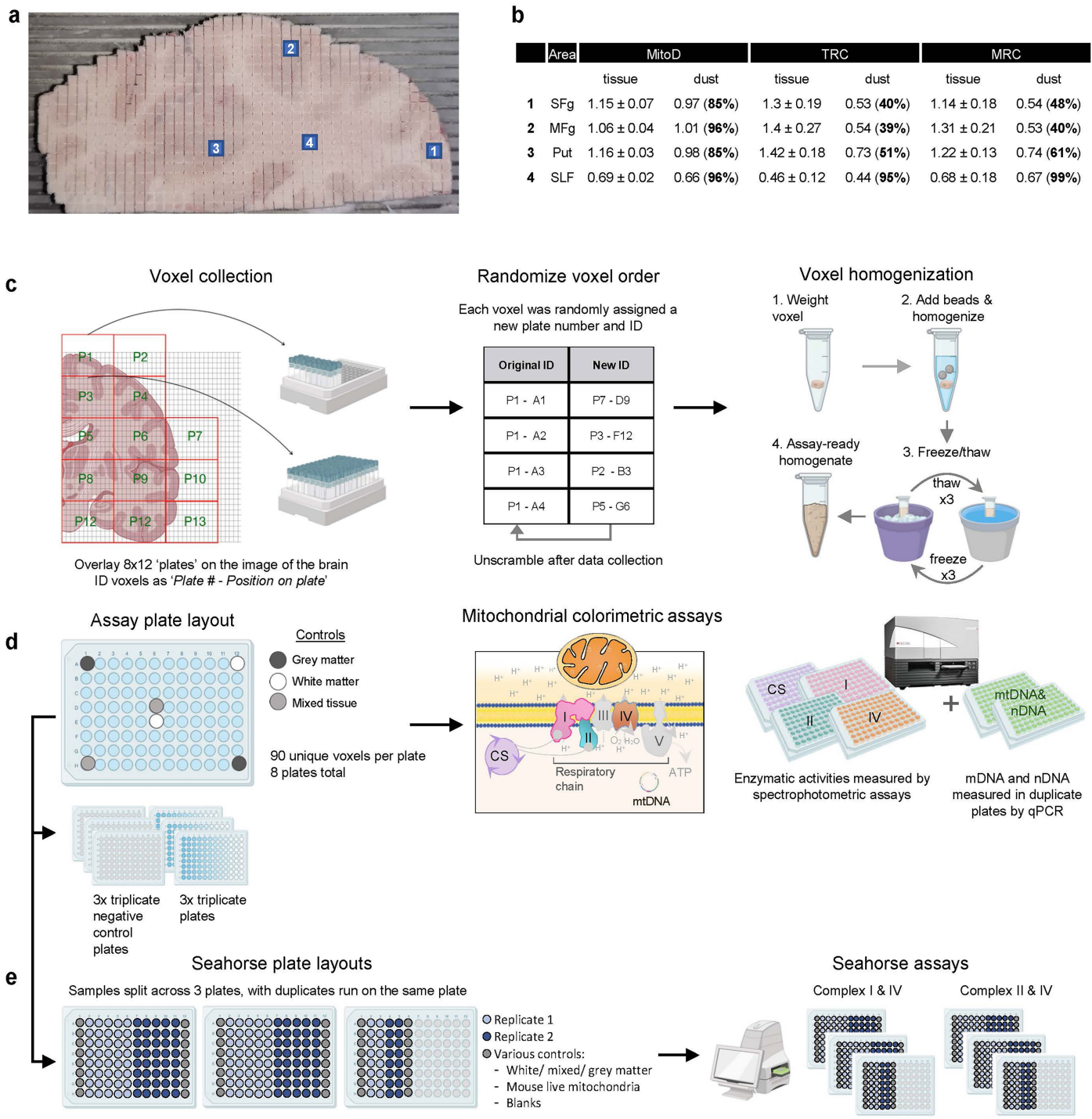


Extended Data Fig. 1 | See next page for caption.

Extended Data Fig. 1 | Workflow of tissue collection. **a**, The right hemisphere coronal slab was mounted on a metal plate with an OCT compound with the top (rostral) surface of the slab parallel to the plate. Created in BioRender. Mosharov, E. (2025) <https://BioRender.com/z524941>. **b**, After affixing the plate to the computer numerical control (CNC) cutting area, the top surface was cleaned with a 12.7 mm flat-tip drill bit rotating at 100 RPM and moving horizontally at 300 mm/sec. After cleaning 1 mm from the top, morphological brain structures were clearly visible and the surface was parallel to the plane of drill bit movement, ensuring that voxels will be of a uniform height. **c**, A 3×3 mm grid was milled with a 0.4 mm drill bit rotating at 10,000 RPM and moving horizontally at 250 mm/min. During a single pass, 0.2 mm of the depth was milled, requiring 15 passes to reach the desired 3 mm of cut depth and a total distance of ~70 m. Total milling time for a 130.8×61.25 mm hemisphere was 4 h and 38 min. **d**, Fully milled slab

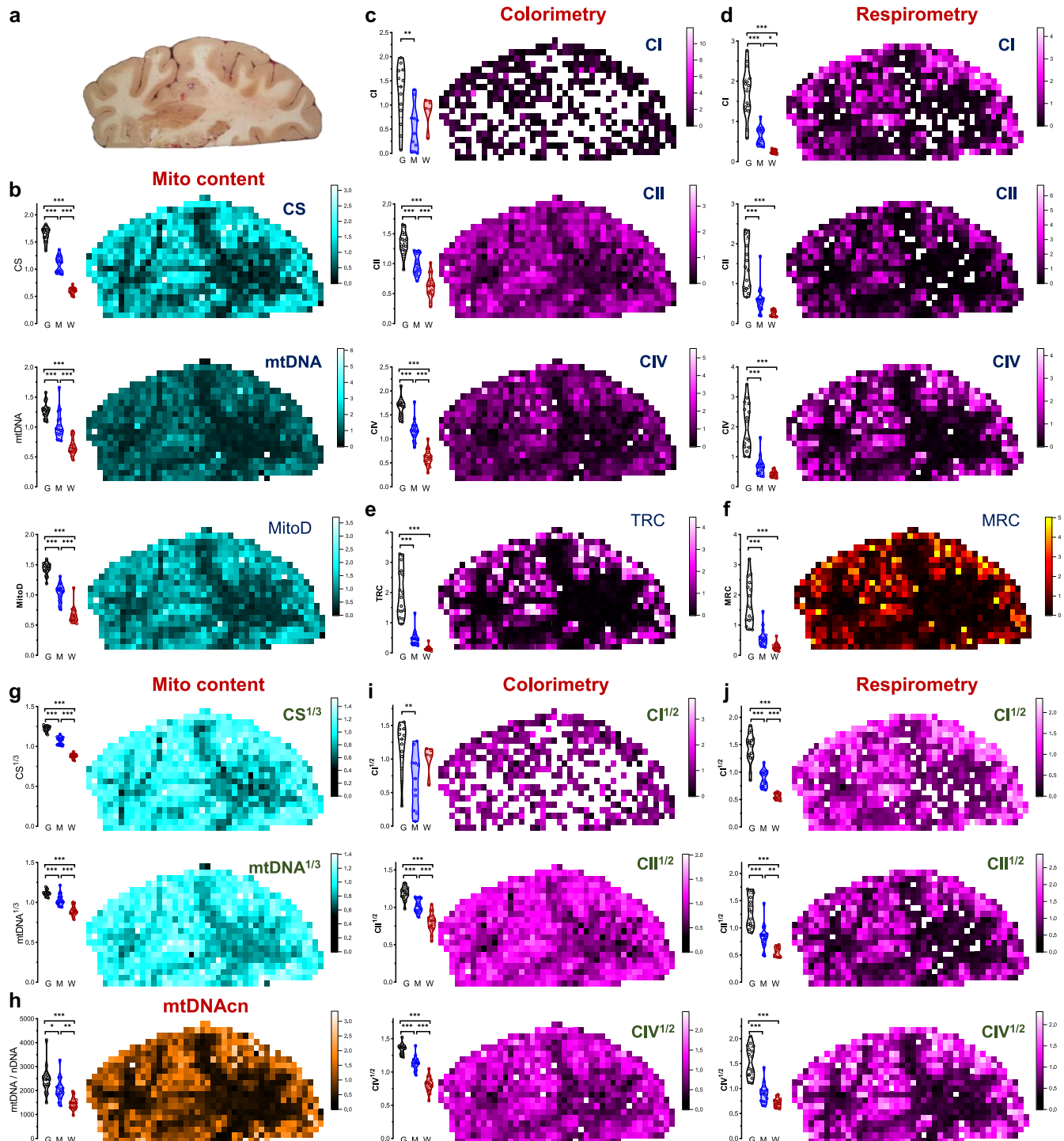
was placed on dry ice. First, four samples of shavings were collected from the surface above one white and three gray areas (Extended Data Fig. 2). Next, shavings were gently removed from the surface with a brush and a pre-chilled scalpel and forceps were used to collect 703 individual voxels. **e**, Following sample collection, slab surface was cleaned once more with a 12.7 mm drill bit. **f**, The metal plate with the slab was then mounted on a freezing microtome and several 50 μm -thick cryosections were collected for histological evaluation. **g**, Summary of the steps during the collection of brain voxels and thin sections. Letters on the right refer to images shown on the corresponding panels. **h** and **i**, Thin brain section stained with Nissl to show neurons and glia either alone (h) or in combination with an immunostaining against neuronal nuclear antigen NeuN to highlight neuron-enriched areas (i).

Article



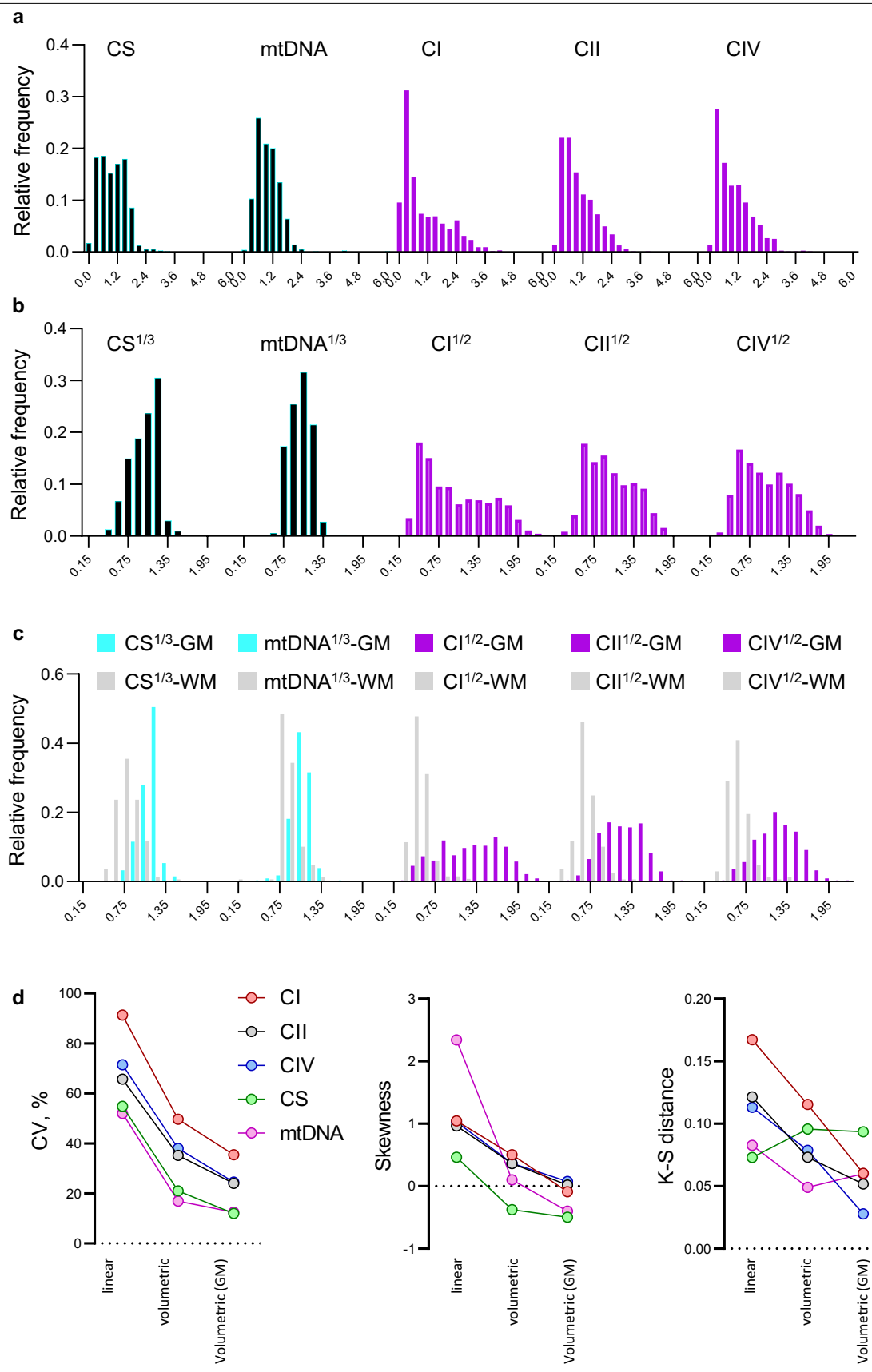
Extended Data Fig. 2 | Analysis of tissue shavings and the workflow for mitochondrial colorimetric and respiratory assays. **a**, Positions of collection sites of the four tissue shavings. Samples 1–3 were above the grey matter areas, while 4 was above a white matter area. **b**, Comparison of mitochondrial activities between the four 'dust' samples and corresponding tissue samples collected below after tissue voxelization. Values are mean ± SD. While all mitochondrial features (MitoD, TRC and MRC) were lower in all dust samples compared to tissue collected below, MitoD was less different between brain dust and tissue block. In sample 4, brain dust and voxels features appear to be very similar,

but this possibly indicates that colorimetry and respirometry assays are at their detection limit when measuring mitochondrial complex activities in the white matter. **c**, Brain voxel collection and preparation. **d**, Voxel plating and data collection for colorimetric mitochondrial assay and qPCR. **e**, Frozen tissue respirometry plate layouts derived from the assay plates on **d** to accommodate all samples and ran in duplicate. Samples were loaded into Seahorse plates at a constant volume rather than constant protein content. Parts **c–e** created in BioRender. Rosenberg, A. (2025) <https://Biorender.com/k26p643>.



Extended Data Fig. 3 | Raw and transformed mitochondrial features measured by colorimetric and respirometry assays. **a**, Image of the brain slab before voxelization. **b**, Distributions of non transformed values (i.e., values are in a linear scale) of citrate synthase (CS) activity, mitochondrial DNA (mtDNA) density and mitochondrial density (MitoD). **c** and **d**, Mapping of mitochondria complexes I, II and IV activities measured by colorimetry (**c**) and respirometry (**d**) assays. **e** and **f**, Tissue Respiratory Capacity (TRC) and Mitochondria Respiratory Capacity (MRC) calculated from raw (non-transformed) values of enzymatic activities. Same maps derived from power transformed values are shown on Fig. 2b-d. **g-j**, Distributions of power transformed values for CS

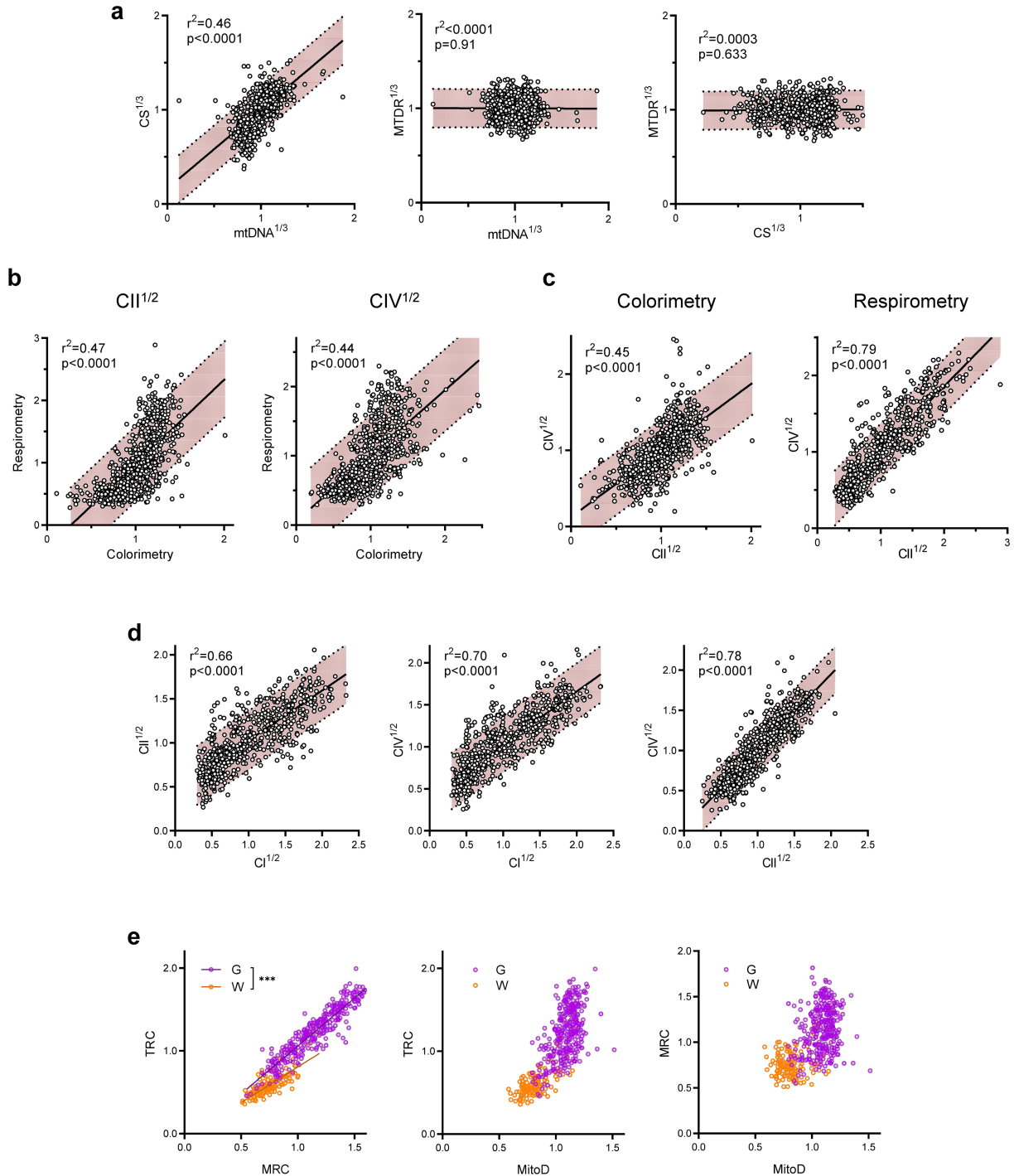
activity and mtDNA density (**g**) mtDNA copy number (mtDNAcn) derived as a ratio of mitochondrial over nuclear DNA (mtDNA/nDNA; **h**), and CI, CII and CIV activities measured by colorimetry (**i**) and respirometry (**j**) assays. Because of the high variability of CI activities measured by colorimetry (**c** and **i**), these data were not used for TRC calculation. All values except mtDNAcn are normalized to each group's mean. Bar graphs on the left of each panel show distributions of repeated measures of control Gray, White and Mixed matter samples on different assay plates (i.e., data points are technical replicates). *** P < 0.05, 0.01 and 0.001 by 1-way ANOVA with Tukey's post-hoc.



Extended Data Fig. 4 | See next page for caption.

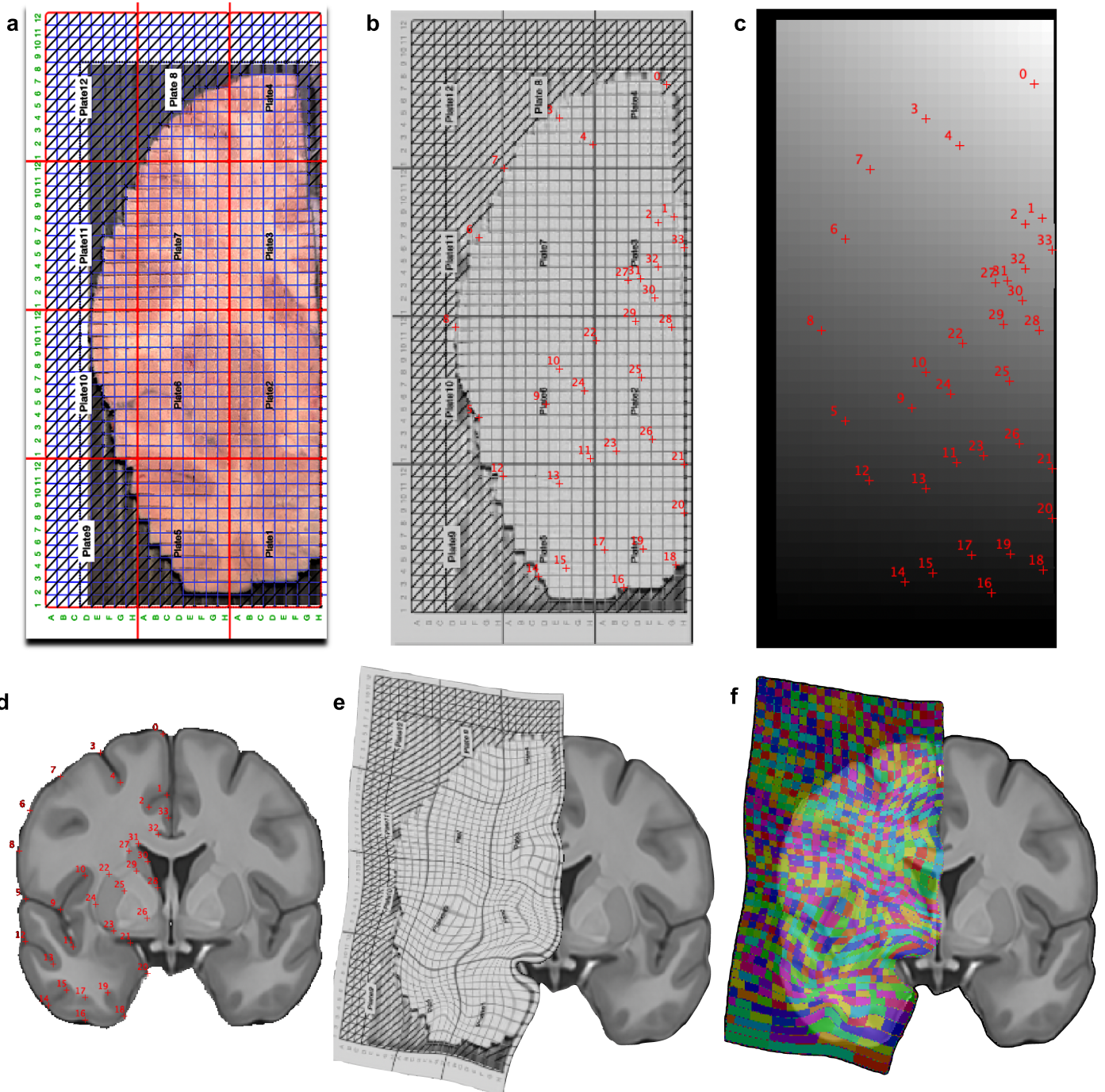
Extended Data Fig. 4 | Volumetric transformation of mitochondrial parameters normalizes their distributions. **a**, Distributions of complexes I, II and IV activities, CS activity and mtDNA density. Complex activities are averages from colorimetry and respirometry assays. **b**, Volumetric transformations of the data on *a*. Mitochondria density metrics and OxPhos complexes activities were calculated as averages of cube root and square root values from colorimetric and respirometry assays. **c**, Same data as *b* with voxels assigned to Gray matter (G, n = 339) and White matter (W, n = 169) clusters based on their anatomical location. Voxels with mixed identity (n = 194) are not shown for simplicity. **d**, Coefficient of variation (CV), skewness and Kolmogorov-Smirnov (K-S) distance of distributions of raw and transformed mitochondrial values from *a-c*.

Article



Extended Data Fig. 5 | Correlations between mitochondrial parameters assayed using different techniques. **a**, CS activity and mtDNA density, which are both related to mitochondria mass, are positively correlated. Because of the high variability in MitoTracker Deep Red measurements (MTDR, a far-red fluorescent probe used to chemically mark and visualize mitochondria in cells), they correlated poorly with CS and mtDNA, thus MTDR was not used for further analysis. **b** and **c**, Relationship between CII and CIV activities measured by

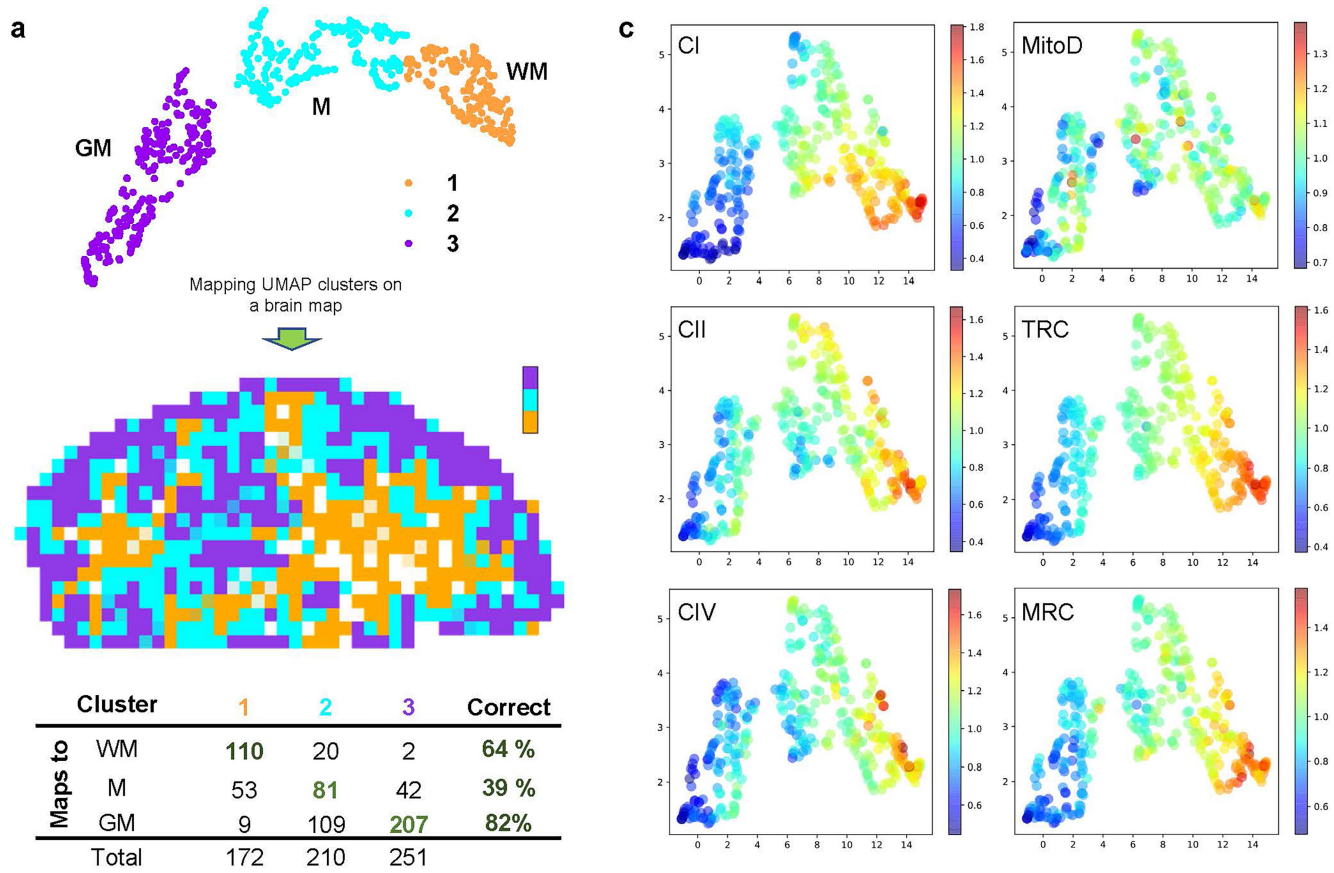
colorimetric and respirometry assays. **d**, Correlations between CI, CII and CIV activities (an average between colorimetric and respirometry assays). **a-d**, Pearson's r^2 values show how well datapoints follow the linear regression; p values indicate if the slope of the regression line is significantly different from zero; shaded areas represent 90% confidence interval. **e**, Relationship between TRC, MRC and MitoD values (see Fig. 2a for definitions) in gray and white matter voxels. *** - the slopes of linear regressions are different with $p < 0.001$.



Extended Data Fig. 6 | Morphing the partitioned brain slice into Montreal Neurological Institute (MNI) space. **a**, Image of the partitioned brain slice with an overlaid milling grid. **b**, Conversion of the brain slice into Neuroimaging Informatics Technology Initiative (NIfTI) format and identification of 34 anatomical landmarks (see below). **c**, Manual creation of NIfTI grid corresponding to the milling grid with the same coordinates. **d**, Identification of the anatomical landmarks as on **b** in the magnetic resonance imaging stereotaxic space (MNI152). **e**, Warping and deformation of the coordinates from **b** to **d**. **f**, Application of this deformation to **c** displayed in color onto the MNI152 for visual convenience. The following 34 anatomical landmarks were identified: top of the interhemispheric fissure (0), surface (1) and deepest point (2) of the cingulate sulcus, surface (3) and deepest point (4) of the superior frontal sulcus (6), middle of the middle frontal gyrus (7), surface of the inferior frontal sulcus, middle surface of the inferior frontal gyrus (8), surface (5) and deepest point (9) of the lateral fissure, highest (10) and lowest point (11) of the circular insular sulcus, surface (12) and deepest point (13) of the superior temporal sulcus, surface (14) and deepest point (15) of the inferior temporal sulcus, surface (16) and deepest point (17) of the accessory temporopolar sulcus, surface (18) and deepest point (19) of the entorhinal sulcus, middle of the entorhinal cortex (20), most medial points of the amygdala (21), superior (22), inferior (23), lateral (24), and medial (25) putamen, most medial internal globus pallidus inferior (26), superior (27), inferior (28) lateral (29) and medial (30) caudate, highest point of the lateral ventricles (31), deepest point of the callosal sulcus (32) and middle of the cingulum gyrus (33).

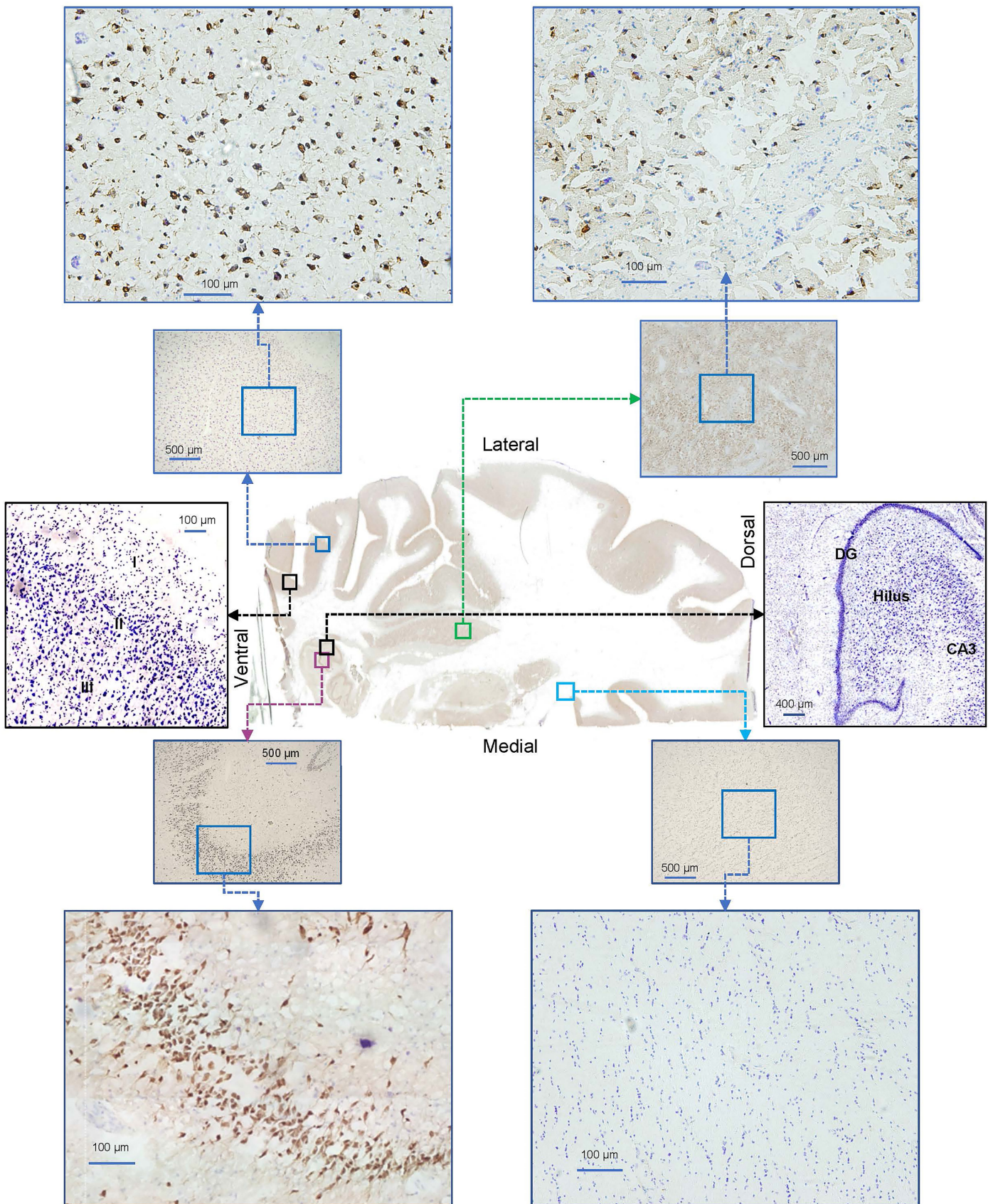
frontal sulcus (6), middle of the middle frontal gyrus (7), surface of the inferior frontal sulcus, middle surface of the inferior frontal gyrus (8), surface (5) and deepest point (9) of the lateral fissure, highest (10) and lowest point (11) of the circular insular sulcus, surface (12) and deepest point (13) of the superior temporal sulcus, surface (14) and deepest point (15) of the inferior temporal sulcus, surface (16) and deepest point (17) of the accessory temporopolar sulcus, surface (18) and deepest point (19) of the entorhinal sulcus, middle of the entorhinal cortex (20), most medial points of the amygdala (21), superior (22), inferior (23), lateral (24), and medial (25) putamen, most medial internal globus pallidus inferior (26), superior (27), inferior (28) lateral (29) and medial (30) caudate, highest point of the lateral ventricles (31), deepest point of the callosal sulcus (32) and middle of the cingulum gyrus (33).

Article



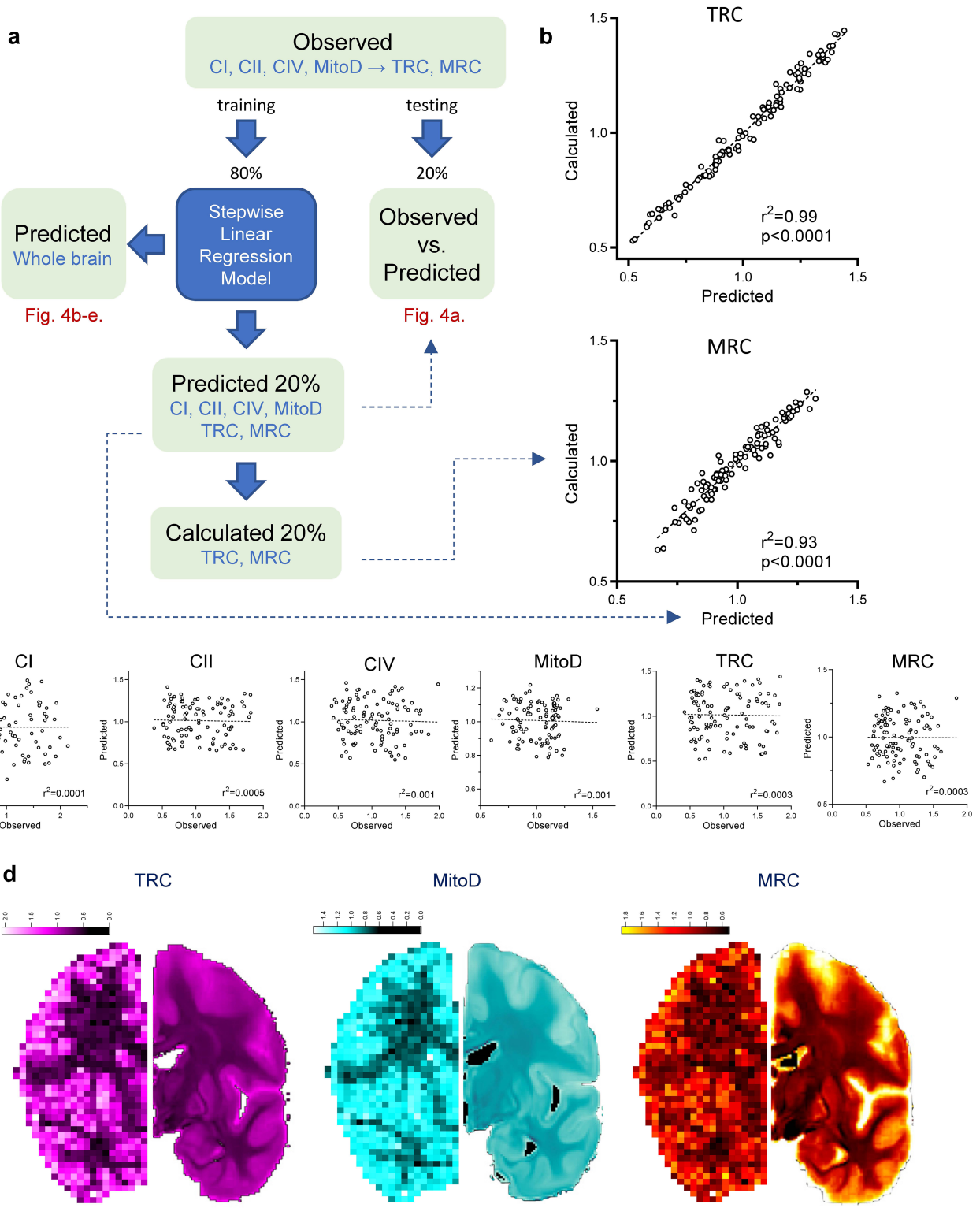
Extended Data Fig. 7 | Clustering of brain voxels by similarities of mitochondrial density and OxPhos activities. **a**, Three visually defined UMAP clusters (upper) obtained after dimensionality reduction of mitochondrial features of all brain voxels (Fig. 2e) were used to predict whether voxels originated from GM, WM or a mixed sample (middle). The table lists prediction accuracy with the number of voxels identified as each type and the fractions that were identified correctly. Note that most localization errors occurred due to the

presence of voxels with mixed composition, which complicates their anatomical mapping. $\chi^2(2, N = 1031) = 10.3, p < 0.01$. **b**, Both MitoD and TRC values were higher in GM than the WM voxels (same data as on Fig. 2f; mean \pm SD), but the TRC decreases more than MitoD. *** $P < 0.0001$ by 2-way ANOVA ($F_{1,1260} = 18.67$). **c**, Distribution of z-score values of each mitochondrial feature on the UMAP plot of GM voxels only (Fig. 2g).



Extended Data Fig. 8 | Histological evaluation of brain areas used for snRNAseq analysis. Staining of 50 μm sections obtained after brain voxelization (see Extended Data Fig. 1) with Nissl stain (blue, neurons and glial cells) and NeuN (brown, neuronal cells). Two panels in black frames show

Nissl-only stained sections with annotated cortical (layers I-II) and hippocampal (dentate gyrus, hilus and CA3) areas. The entire Nissl-stained brain section is shown on Extended Data Fig. 1h.



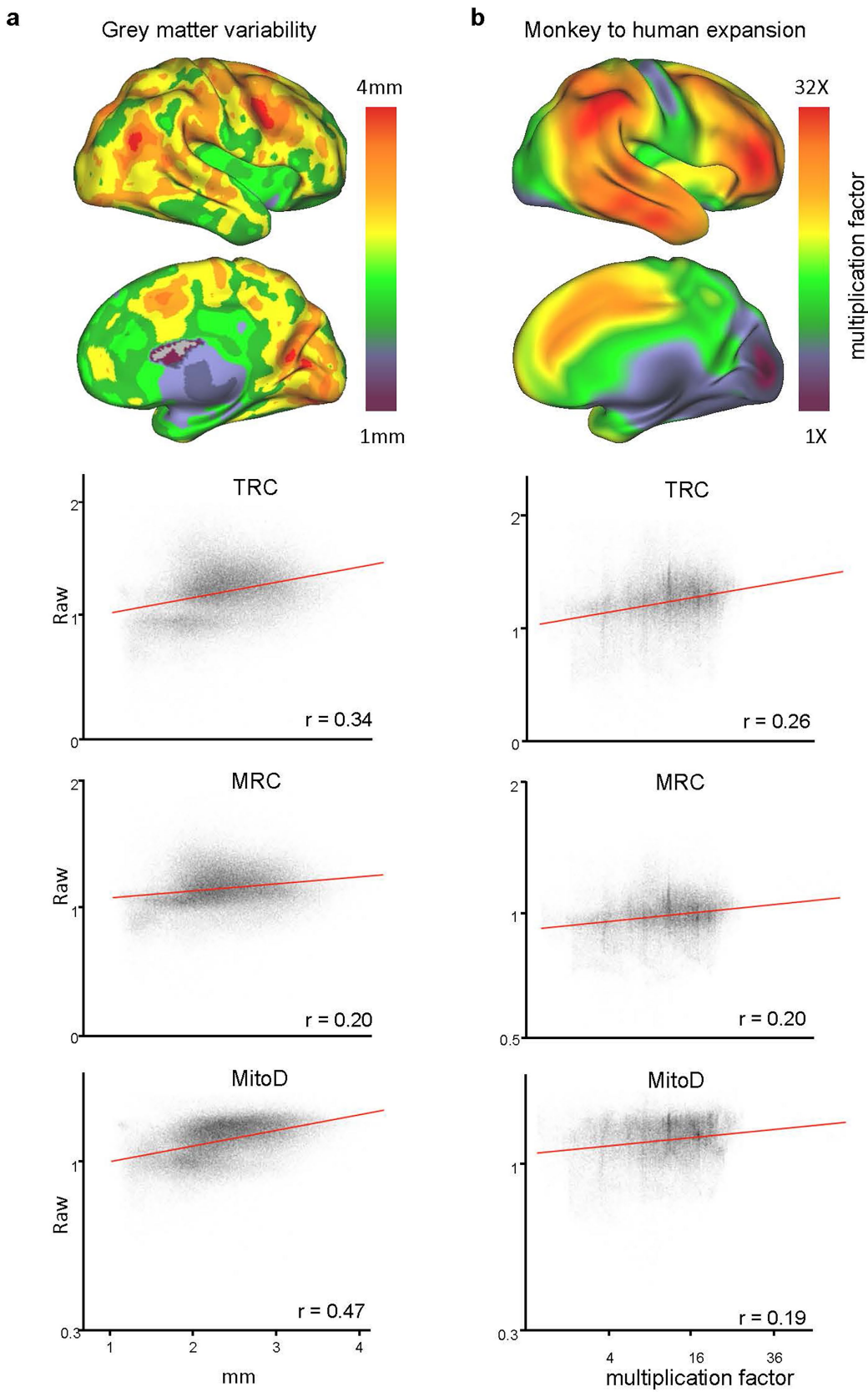
Extended Data Fig. 9 | See next page for caption.

Extended Data Fig. 9 | Workflow of data processing with stepwise linear regression model.

a. Voxels that had all 6 mitochondrial parameters (4 independent and 2 derived) and with a sum of GM and WM probabilities more than 70% ($n = 539$ ‘observed’ voxels) were randomly split into 80% training ($n = 431$) and 20% testing ($n = 108$) datasets. A model was built by predicting each of the 6 mitochondrial values in the training dataset using stepwise backward linear regression of neuroimaging values (Extended Data Table 1). The model was then applied to the testing dataset to verify predictions accuracy. Correlations between observed and predicted values of the testing dataset are shown on Fig. 4a. Next, the predictive model was extended to all the brain voxels of the MNI space to produce a whole brain estimated map for each of the mitochondrial values (Fig. 4b–e). **b.** Correlation between TRC and MRC

values either predicted by the model or calculated from predicted CI, CII, CIV and MitoD values (see formulas on Fig. 2a). Strong correlation between predicted and calculated values for TRC and MRC shows the robustness of the model as it can accurately predict derived parameters (TRC and MRC) without the knowledge of the independent parameters they were derived from (CI, CII, CIV and MitoD). **c.** Scatterplots of 20% out-of-sample prediction of mitochondrial profiles (same data as on Fig. 4a) after the pairing between voxels observed and predicted values was scrambled. Slopes of all linear regressions are not different from zero ($p > 0.7$; Pearson’s r^2 is shown on each graph). **d.** Predicted (right) vs. observed (left, same as Fig. 2b–d) maps of TRC, MitoD and MRC values from the same coronal plane. Both sides show the right hemisphere (i.e., the predicted image is mirrored). Scale bars are in z-score units.

Article



Extended Data Fig. 10 | Higher mitochondrial activity in phylogenetically younger brain areas. a–b, Comparison between predicted mitochondrial parameters (raw TRC, MRC and MitoD values for 80,0039 brain voxels) and

indirect measures of brain evolution such as grey matter variability (a) and monkey-to-humans areal expansion (b).

Extended Data Table 1 | List of neuroimaging metrics and their standardized beta coefficient relationship with the mitochondrial features indicating the unique contribution of each predictor while accounting for the influence of all other variables in the model

| | Abbreviation | MRI metric | CI | CII | CIV | MitoD | TRC | MRC |
|----------------|--------------|---|--------|-------|--------|-------|--------|-------|
| Diffusion MRI | AD | axial water diffusivity | | .242 | | | .246 | |
| | FA | fractional anisotropy (white matter density) | | | .681 | .820 | | |
| | RD | radial water diffusivity | -.365 | | .439 | .632 | | -.175 |
| | StreDensity | streamlines density | | | -.184 | | | |
| | ICVF | intra-cellular volume fraction | -.371 | | | | | |
| | ISOCF | extra-cellular volume fraction | | -.158 | -.438 | -.445 | -.330 | |
| | MD | mean water diffusivity | | | | | | |
| Structural MRI | ODI | orientation dispersion index (neurite complexity) | .363 | .323 | .628 | .499 | .481 | .334 |
| | T1W | T1w imaging | | | | | | |
| | T2W | T2w imaging | -.245 | -.304 | -.458 | -.410 | -.330 | -.244 |
| | T1w/T2w | T1w/T2w ratio | -.656 | -.580 | -.723 | -.622 | -.617 | -.593 |
| | FLAIR | imaging approach to see the anatomy of the brain | -.273 | -.221 | | | -.339 | |
| | CT | cortical thickness | | | | | | |
| | inner_CSA | local surface for inner cortical ribbon | | | | | | |
| Functional MRI | plial_CSA | local surface for outer cortical ribbon | | | | | | |
| | GM | probability of gray matter | -1.038 | | -1.382 | | -1.177 | -.939 |
| | WM | probability of white matter | -1.082 | | -1.263 | -.312 | -1.040 | -.906 |
| | Max_activity | maximum bold derived from fMRI | | | .380 | | .333 | .501 |
| | Reho | regional homogeneity | | .145 | | | .135 | |
| | Entropy | synaptic complexity derived from fMRI | | | | -.386 | | -.365 |
| | ALFF | amplitude of Low-Frequency Fluctuation | | | | | | -.560 |
| | fALFF | ratio between low and and high frequency fluctuations | | | | | | |

Reporting Summary

Nature Portfolio wishes to improve the reproducibility of the work that we publish. This form provides structure for consistency and transparency in reporting. For further information on Nature Portfolio policies, see our [Editorial Policies](#) and the [Editorial Policy Checklist](#).

Statistics

For all statistical analyses, confirm that the following items are present in the figure legend, table legend, main text, or Methods section.

n/a Confirmed

- The exact sample size (n) for each experimental group/condition, given as a discrete number and unit of measurement
- A statement on whether measurements were taken from distinct samples or whether the same sample was measured repeatedly
- The statistical test(s) used AND whether they are one- or two-sided
Only common tests should be described solely by name; describe more complex techniques in the Methods section.
- A description of all covariates tested
- A description of any assumptions or corrections, such as tests of normality and adjustment for multiple comparisons
- A full description of the statistical parameters including central tendency (e.g. means) or other basic estimates (e.g. regression coefficient) AND variation (e.g. standard deviation) or associated estimates of uncertainty (e.g. confidence intervals)
- For null hypothesis testing, the test statistic (e.g. F , t , r) with confidence intervals, effect sizes, degrees of freedom and P value noted
Give P values as exact values whenever suitable.
- For Bayesian analysis, information on the choice of priors and Markov chain Monte Carlo settings
- For hierarchical and complex designs, identification of the appropriate level for tests and full reporting of outcomes
- Estimates of effect sizes (e.g. Cohen's d , Pearson's r), indicating how they were calculated

Our web collection on [statistics for biologists](#) contains articles on many of the points above.

Software and code

Policy information about [availability of computer code](#)

Data collection Supplementary Files 2&3 contain Igor Pro routines used for brain partitioning, sample randomization and de-randomization

Data analysis Supplementary File 1 contains the markdown of the RNAseq analysis, which was done in Python.
Supplementary File 4 contains the Python code used for the conversion of the image of the brain slab to Neuroimaging Informatics Technology Initiative (NIfTI) format.
Data was analyzed and graphed using Igor Pro (Wavemetrics, Lake Oswego, OR; RRID:SCR_000325), Python Programming Language (RRID: SCR_008394) and Prism 8.0 software (GraphPad Software Inc, San Diego, CA; RRID:SCR_002798).

For manuscripts utilizing custom algorithms or software that are central to the research but not yet described in published literature, software must be made available to editors and reviewers. We strongly encourage code deposition in a community repository (e.g. GitHub). See the Nature Portfolio [guidelines for submitting code & software](#) for further information.

Data

Policy information about [availability of data](#)

All manuscripts must include a [data availability statement](#). This statement should provide the following information, where applicable:

- Accession codes, unique identifiers, or web links for publicly available datasets
- A description of any restrictions on data availability
- For clinical datasets or third party data, please ensure that the statement adheres to our [policy](#)

Provide your data availability statement here.

Research involving human participants, their data, or biological material

Policy information about studies with [human participants or human data](#). See also policy information about [sex, gender \(identity/presentation\), and sexual orientation](#) and [race, ethnicity and racism](#).

Reporting on sex and gender

Brain donor sex (male) was self-reported. Sex/gender were not considered in the study design. A single brain for the study was chosen based on its toxicological and neurological records, short postmortem interval and age of the donor at the time of death.

Reporting on race, ethnicity, or other socially relevant groupings

n/a

Population characteristics

n/a

Recruitment

n/a

Ethics oversight

New York State Psychiatric Institute, New York, NY, USA

Note that full information on the approval of the study protocol must also be provided in the manuscript.

Field-specific reporting

Please select the one below that is the best fit for your research. If you are not sure, read the appropriate sections before making your selection.

Life sciences Behavioural & social sciences Ecological, evolutionary & environmental sciences

For a reference copy of the document with all sections, see nature.com/documents/nr-reporting-summary-flat.pdf

Life sciences study design

All studies must disclose on these points even when the disclosure is negative.

Sample size

This proof-of-principle study was performed on a frozen coronal hemisphere from a single donor brain. Number of voxels/samples was based on the physical size of the brain slab, which was partitioned at 3x3x3mm resolution, similar to MRI resolution. This yielded 703 samples and required >20,000 independent assays to measure mitochondria abundance and OxPhos enzyme activities.

Data exclusions

Some voxels/samples were excluded from the analysis due to 1) missing readouts from some of the assays, due to technical or sensitivity issues, or 2) imperfect transformation of the physical voxels into the MNI space, which resulted in some of them having less than 70% of gray +white matter.

Replication

Assays for mitochondria abundance and OxPhos enzyme activities were performed in duplicates or triplicates.

Randomization

All samples/voxels were randomly assigned to 96-well assay plates by a locally written Igor Pro routine available in Supplementary Data2&3.

Blinding

To minimize potential batch effects and to blind the experimenter to the origin of the voxel, samples were scrambled using an Igor Pro routine: unique coordinates of each sample on the brain map were substituted with new, randomly generated coordinates on 96-well assay plates.

Reporting for specific materials, systems and methods

We require information from authors about some types of materials, experimental systems and methods used in many studies. Here, indicate whether each material, system or method listed is relevant to your study. If you are not sure if a list item applies to your research, read the appropriate section before selecting a response.

Materials & experimental systems

| | |
|-------------------------------------|-------------------------------|
| n/a | Involved in the study |
| <input checked="" type="checkbox"/> | Antibodies |
| <input checked="" type="checkbox"/> | Eukaryotic cell lines |
| <input checked="" type="checkbox"/> | Palaeontology and archaeology |
| <input checked="" type="checkbox"/> | Animals and other organisms |
| <input checked="" type="checkbox"/> | Clinical data |
| <input checked="" type="checkbox"/> | Dual use research of concern |
| <input checked="" type="checkbox"/> | Plants |

Methods

| | |
|-------------------------------------|------------------------|
| n/a | Involved in the study |
| <input checked="" type="checkbox"/> | ChIP-seq |
| <input checked="" type="checkbox"/> | Flow cytometry |
| <input type="checkbox"/> | MRI-based neuroimaging |

Plants

Seed stocks

Report on the source of all seed stocks or other plant material used. If applicable, state the seed stock centre and catalogue number. If plant specimens were collected from the field, describe the collection location, date and sampling procedures.

Novel plant genotypes

Describe the methods by which all novel plant genotypes were produced. This includes those generated by transgenic approaches, gene editing, chemical/radiation-based mutagenesis and hybridization. For transgenic lines, describe the transformation method, the number of independent lines analyzed and the generation upon which experiments were performed. For gene-edited lines, describe the editor used, the endogenous sequence targeted for editing, the targeting guide RNA sequence (if applicable) and how the editor was applied.

Authentication

Describe any authentication procedures for each seed stock used or novel genotype generated. Describe any experiments used to assess the effect of a mutation and, where applicable, how potential secondary effects (e.g. second site T-DNA insertions, mosaicism, off-target gene editing) were examined.

Magnetic resonance imaging

Experimental design

Design type

Template based multimodal imaging

Design specifications

We used neuroimaging templates derived from 2 databases (Human Connectome Project and Ishare) to produce a predictive model of the mitochondrial brain features

Behavioral performance measures

N/A

Acquisition

Imaging type(s)

Structural, Diffusion and task (free movie watching) and resting state fMRI

Field strength

3T & 7T

Sequence & imaging parameters

Parameters for the free movie watching task fMRI are reported in <https://www.humanconnectome.org/hcp-protocols-ya-7t-imaging>, T1w and T2w imaging at <https://www.humanconnectome.org/hcp-protocols-ya-3t-imaging>, Diffusion and resting state fMRI parameters in Tsuchida, A. et al. The MRI-Share database: brain imaging in a cross-sectional cohort of 1870 university students. Brain Struct. Funct. 226, 2057–2085 (2021).

Area of acquisition

Whole brain

Diffusion MRI

Used

Not used

Parameters Parameters of acquisitions are reported in Tsuchida, A. et al. The MRI-Share database: brain imaging in a cross-sectional cohort of 1870 university students. Brain Struct. Funct. 226, 2057–2085 (2021).

Preprocessing

Preprocessing software

FSL, MRtrix, ANTs

Normalization

Diffeomorphic

Normalization template

MNI152

Noise and artifact removal

N/A

Volume censoring

N/A

Statistical modeling & inference

| | |
|---|--|
| Model type and settings | N/A |
| Effect(s) tested | N/A |
| Specify type of analysis: | <input checked="" type="checkbox"/> Whole brain <input type="checkbox"/> ROI-based <input type="checkbox"/> Both |
| Statistic type for inference | N/A |
| (See Eklund et al. 2016) | |
| Correction | N.A |

Models & analysis

| | |
|---|---|
| n/a | Involved in the study |
| <input checked="" type="checkbox"/> | <input type="checkbox"/> Functional and/or effective connectivity |
| <input checked="" type="checkbox"/> | <input type="checkbox"/> Graph analysis |
| <input type="checkbox"/> | <input checked="" type="checkbox"/> Multivariate modeling or predictive analysis |
| Multivariate modeling and predictive analysis | Independent variables are values for axial diffusivity, fractional anisotropy , radial diffusivity, streamlines density, intracellular volume fraction, extracellular volume fraction, mean diffusion, orientation dispersion index, T1w, T2w, T1w/T2w, FLAIR, cortical thickness, inner cortical surface area, outer cortical surface area, probability of grey and white matter, fMRI maximum activity during free movie watching , shannon entropy during free movie watching, regional homogeneity at rest, amplitude of low-frequency fluctuation, ratio between low and and high frequency fluctuations. Dependant variables were Cl, CII, CIV, MitoD, TRC and MRC. |